UNIVERSITÀ DEGLI STUDI DI PADOVA

"Galileo Gallilei" Department of Physics and Astronomy

Master's Degree in Astrophysics and Cosmology

Final dissertation

Interferometric Measurements and Analysis of Thermal Noise in Solids

Candidate: Alexander Fahlman

Thesis Supervisor: Giacomo Ciani

Thesis Co-Supervisor: Livia Conti

Thesis Co-Supervisor: Marco Bazzan

Academic Year 2024/2025

Contents

Introduction

Thermal noise is one of the main sources of noise that limits sensitivity in high-sensitivity applications. One of the applications significantly limited by thermal noise today is the detection of gravitational waves. In the current generation of ground-based gravitational wave detectors thermal noise is one of the largest contributors to the noise budget, and at some frequencies it is the single largest source of noise; in some detectors it is the largest noise source at frequencies in the few hundreds of hertz, which is the range of greatest interest for current gravitational wave detections [1]. The current approach to modeling thermal noise in gravitational wave detectors is to treat the detector as if it were in thermodynamic equilibrium and use the fluctuation dissipation and equipartition theorems, which are valid in thermodynamic equilibrium only. However, real detectors are not in thermodynamic equilibrium because of heat flux due to laser light absorption in the mirrors and suspensions, heating systems that compensate for optical aberrations from thermal effects, and, in future detectors, the operation of mirrors at cryogenic temperatures. There is as yet no complete theory of spontaneous fluctuations in solids out of thermodynamic equilibrium, which would be required to model such a system.

The aim of the Non-Equilibrium Thermal Noise (NETN) experiment is to investigate the thermal noise to help develop a model that can provide a phenomenological relation between the behavior of the thermal noise and other parameters that characterize the non-equilibrium state. This will be done using an aluminum mechanical oscillator system that is isolated from external noise using a mechanical suspension and by keeping it under vacuum where it is kept in non-equilibrium steady states using heat fluxes. The oscillator motion that is induced by thermal noise will be investigated using a quadrature phase differential interferometer in which the oscillator is used as one of the mirrors for the interferometer. Measurements will be made both in equilibrium states and non-equilibrium steady states from creating a thermal gradient across the oscillator.

Section 1 provides a theoretical background on gravitational wave generation and detection in interferometric observatories. Noise sources in gravitational wave detectors and a the current method of dealing with thermal noise in thermodynamic equilibrium, and attempts to characterize thermal noise out of thermodynamic equilibrium are then discussed. The experimental setup is presented in chapter 2. In chapter 3 data analysis is discussed, detailing both the ideal functioning of the quadrature phase differential interferometer, and how we compensate for the non ideal behavior of experimental components. This chapter also shows how we infer the effective noise temperature of the oscillator using the spectral analysis of the data. Chapter 4 summarizes various changes and upgrades that were made to the experimental setup during this work. And finally, chapter 5 discusses the analytical results of this work and the progress made towards being able to characterize thermal noise out of thermodynamic equilibrium.

1 Gravitational Wave Detectors and Noise

1.1 Gravitational Wave Theory

Gravitational waves (GW) are distortions in the curvature of spacetime that propagate as waves at the speed of light. GW are generated by the asymmetric acceleration of large masses, with observable GW only being created in some extreme astrophysical systems. They are a prediction of Albert Einstein's general theory of relativity. The first mathematical description of GW came from a paper published by Einstein in 1916 [2]. In this paper, Einstein linearized his field equation such that weak gravitational fields could be described as:

$$g_{\mu\nu} = \eta_{\mu\nu} + h_{\mu\nu} \tag{1.1}$$

where $h_{\mu\nu}$ describes a perturbation in the flat metic that represents the gravitational wave, such that $|h << 1|$, where $\eta_{\mu\nu}$ is the flat metric. Einstein showed that it was possible for them to transport energy and so be detectable according to general relativity. For the linearized Einstein equation one can obtain a wave equation that describes the perturbation.

$$\Box h^{\mu\nu} = \left(-\frac{\partial^2}{\partial t^2} + \nabla^2\right) h^{\mu\nu} = -\frac{16\pi G}{c^4} T^{\mu\nu} \tag{1.2}$$

where G is the gravitational constant, c is the speed of light, and $T^{\mu\nu}$ is the stress-energy tensor that describes the density and flux of energy and momentum in spacetime.

For the purposes of this discussion, and often in literature, it is useful to describe GW in the transverse-traceless gauge (TT gauge). For a GW propagating in the z-direction, the perturbation can be described as:

$$h_{ij}(t,x,y,z) = \begin{pmatrix} 0 & 0 & 0 & 0 \\ 0 & h_+ & h_\times & 0 \\ 0 & h_\times & -h_+ & 0 \\ 0 & 0 & 0 & 0 \end{pmatrix} e^{i\omega(t-z/c)} \tag{1.3}$$

where h_+ is the plus-polarization of the GW and $h_\times$ is the cross-polarization. As the name transverse-traceless gauge suggests, the trace of the metric is 0, and the wave propagates as a transverse wave along the z axis. This results in a description of a gravitational wave in which the strain caused by the GW is entirely in the x-y plane as the wave propagates in the z-direction. The effect on spacetime can be expressed as two separate polarizations, the plus and cross-polarizations, and can be visualized in figure 1.1 where we dan see the displacement of a ring of test particles.

We can also discuss the displacement of test particles mathematically. The the x and y directions of the displacement of a test particle due to the plus and cross polarizations of a gravitational wave can be written as:

$$\delta x_+(t) = \frac{h_+}{2} x_0 sin(\omega t) \tag{1.4}$$

$$\delta y_+(t) = -\frac{h_+}{2} y_0 sin(\omega t) \tag{1.5}$$

$$\delta x_\times(t) = \frac{h_\times}{2} y_0 sin(\omega t) \tag{1.6}$$

$$\delta x_\times(t) = \frac{h_\times}{2} x_0 sin(\omega t) \tag{1.7}$$

where δ_x and δ_y represent the displacement in each direction from an initial position x_0 and y_0. The generalized form of the displacement shows that the net force on a single test particle is zero, but the displacement relative to other particles is a real effect that is still described by this system of equations [3].

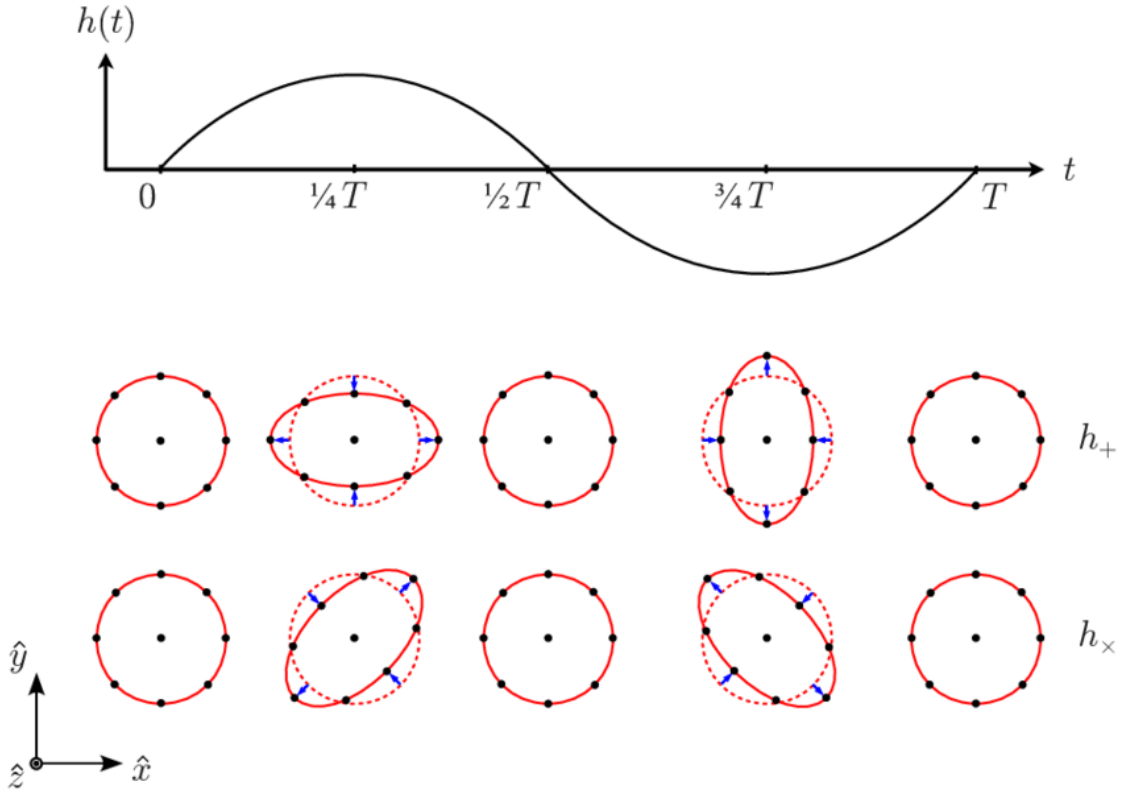

Figure 1.1: This figure shows the effect of the plus (middle row) and cross (lower row) polarizations of a gravitational wave on a system of test particles in the xy plane, as the GW propagates along to z-axis. The top row of the figure shows the total strain of the GW as it completes an entire period. The figure collectively shows how a series of test masses would be distorted from a circular configuration as a gravitational wave passed perpendicularly through the plane they reside in. Figure from [4]

The second derivative of a changing quadrupole moment of a system leads to the generation of gravitational waves. The main astronomical situation of interest in the current generation of detectors is binary systems of massive compact objects such as black holes or neutron stars. These objects produce the strongest gravitational waves of any binary objects due to their large mass and their density which allows them to orbit closer to each other before merging, and so reaching a higher orbital frequency and higher acceleration.

Pairs of binary compact objects will lose energy and inspiral as gravitational waves are emitted from the system. This can be seen easily with the following equation that describes the radius of separation of the binary pair of objects with a circular orbit as a function of time:

$$R(t) = R_0 \left(\frac{t_{coal} - t}{t_{coal} - t_0} \right)^{1/4} \tag{1.8}$$

where R_0 is the radius of separation at a time t_0 and t_{coal} is the time at which the binary

pair coalesces into a single object. When $t << t_{coal}$ the radius of separation changes slowly over time. As t grows the rate at which the radius of separation decays increases at an accelerated pace. This expression is valid until t begins to approach t_{coal} at which time the binary pair enters a phase known as the "final plunge" where the GW frequency f_{gw} increases sharply before coalesence such that:

$$f_{gw}(t_{coal} - t) \simeq 134Hz \left(\frac{1.21M_{\odot}}{M_c}\right)^{5/8} \left(\frac{1s}{t_{coal} - t}\right)^{3/8} \tag{1.9}$$

where $M_{\odot}$ is a solar mass and $M_c = (m_1 m_2)^{3/5}/(m_1 + m_2)^{1/5}$ is the chirp mass, which is an observable of the system based on the masses of the two binary objects m_1 and m_2. As t grows with respect to t_{coal} we see a similar but inverted behavior to what we observed with R. When t is small f_{gw} increases very slowly, but will increase at a faster rate as t grows. When the binary enters the final plunge phase f_{gw} will grow rapidly.

This growth in frequency and decay in radius of separation can be used to show that the amplitude of the gravitational waves for both polarizations also grows at an increasing rate as t begins to approach t_{coal}, with a similar sharp growth in amplitude during the final plunge:

$$h_{+}(t) = \frac{4}{r}\left(\frac{GM_c}{c^2}\right)^{5/3}\left(\frac{\pi f_{\rm gw}}{c}\right)^{2/3}\frac{1+\cos^2\theta}{2}\cos(2\pi f_{\rm gw} t_{\rm ret} + 2\phi) \tag{1.10}$$

$$h_{\times}(t) = \frac{4}{r}\left(\frac{GM_c}{c^2}\right)^{5/3}\left(\frac{\pi f_{\rm gw}}{c}\right)^{2/3}\cos\theta\sin(2\pi f_{\rm gw} t_{\rm ret} + 2\phi) \tag{1.11}$$

where r is the radial distance of the observer from the center of mass of the system (for $r >> R$), θ is the angle between the direction of the observer and the angular velocity vector of the binary system, ϕ is an angle that is a constant that depends on the choice of the time origin, and t_{ret} is the retarded time $t_{ret} = t - r/c$.

Figure 1.2 shows that this behavior of the GW amplitude growing rapidly near coalescence is indeed measured in real observations.

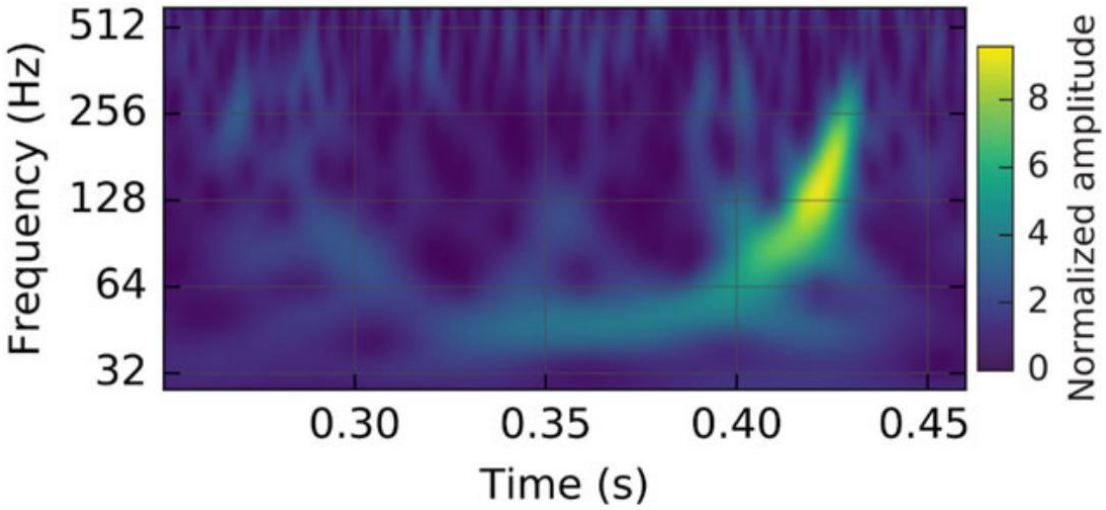

Figure 1.2: This figure shows a plot of gravitational wave frequency f_{gw} versus time with a heatmap of strain measured by the LIGO Hanford detector from the first direct detection of gravitational waves in 2015, referred to as GW150914. This figure shows how the wave amplitude increases sharply in real binary systems just as described by equations 1.9, 1.10, and 1.11. Figure taken from B. P. Abbot et al. 2016 [5].

1.2 Gravitational Wave Detectors

Despite the fact that general relativity had predicted the existence of gravitational waves that transport energy and momentum and so produce measureable effects, the idea that gravitational waves existed and could be detected was met with skepticism when Einstein proposed them in 1915, including by Einstein himself. Even if gravitational waves were a real phenomenon, it was expected to be incredibly challenging, if not impossible, to make actual detections. The first experimental efforts to detect gravitational waves were made by Joseph Weber at the University of Maryland. Weber constructed the first resonant-mass antenna, which was followed by his former Ph.D. student, Robert Forward, constructing the first free-mass laser interferometer antenna [6].

The first indirect detection of gravitational waves was not made until 1975 from observations of pulsars. Physicists Russell Hulse and Joseph Taylor were working on a survey of pulsars at the Arecibo Observatory in Puerto Rico when they made the first detection of a pulsar in a binary system, the 59 ms pulsar PSR 1913+16. Pulsars can be used as highly precise clocks in astronomy because are highly stable both from rotation to rotation and over larger periods of time. This property of pulsars allowed the determination of all of the parameters of the binary needed to calculate the emission of gravitational waves, including the orbital period of this pulsar around its neutron star companion; it also allows the measurement of the orbital decay of the binary. This orbital decay was consistent with predictions of orbital decay from energy dissipation from gravitational wave emission, providing the first indirect evidence of the existence of gravitational waves [7].

The method first pioneered by Forward using free-mass interferometry ultimately resulted in the first detection of gravitational waves in 2015 by the Laser Interferometer Gravitational-wave Observatory (LIGO). This first detection corresponded to a binary black hole merger, and is visualized in figure 1.2.

Resonant Bar Detectors

Resonant bar detectors represent the first attempts at directly detecting gravitational waves. This method was initially developed by Joseph Weber and the first resonant bar detector was constructed in the 1960's at the University of Maryland.

Gravitational waves are a purely non-local phenomena, due to the Equivalence Principle a single particle cannot feel the effects of a gravitational wave. This generally encourages gravitational wave detectors to be larger rather than smaller, since gravitational wave effects are ultimately tidal in nature. Broadly, gravitational wave detectors can come in two different configurations, free-mass, and non-free-mass [6].

Free-mass detectors, which measure the displacement of two separate masses that are free to oscillate, will be discussed in the next section. Resonant bar detectors represented attempts to make a non-free-mass gravitational wave detector. A single rigid object will experience stresses as GW deform the object while they pass through it. By engineering a mass of the appropriate material, size, and shape GW waves of a frequency of interest could be made to excite a resonant mode of the object, amplifying the vibrations induced by a passing GW. Weber's original design would use an object with a high quality factor Q so that the PSD peaks from the excitation of the bar due to gravitational waves would be visible above the background noise, which is dominated by thermal noise. Since thermal noise is stochastic and gravitational wave signals are not, integration over time can differentiate gravitational wave signals from thermal noise. The most sensitive frequencies for detection of gravitational waves from these resonant bar detectors would be around the resonant frequency of the first longitudinal mode of the bar, so that resonant bar detectors with this resonant mode being around 1kHZ would be most sensitive in the detection of supernovae explosions.

In 1969 Weber announced that his experiment had detected a GW signal, but his results were never replicated as no other resonant bar detector has yet confirmed a GW detection. Many other resonant bar detectors were constructed since, with NAUTILUS (figure 1.3a), EXPLORER, and AURIGA (figure 1.3b) reaching some of the highest sensitivities [6]. New generations of detectors ran at cryogenic temperatures to try and further reduce thermal noise to increase sensitivity. NAUTILUS and AURIGA (constructed in Rome and Legnaro, Padua, respectively) had been run as low as ultra-cryogenic temperatures (130mK and 200mK, respectively), while EXPLORER was run at only 2.6K.

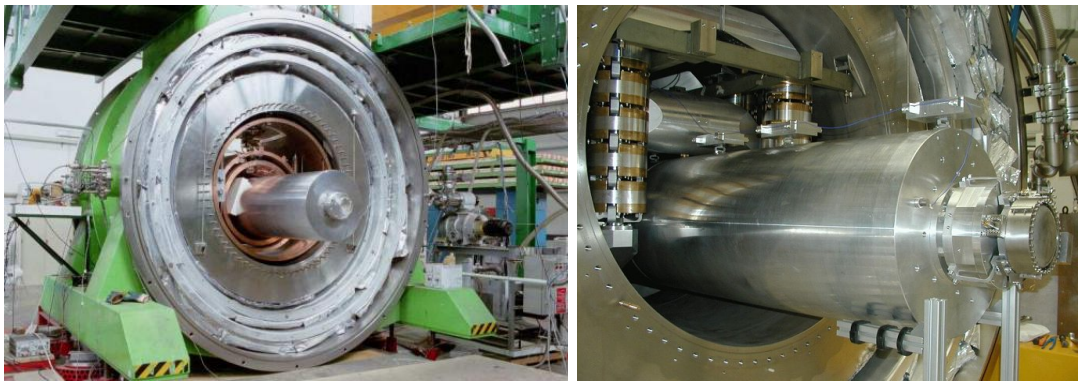

(a) NAUTILUS resonant bar detector (b) AURIGA resonant bar detector

Figure 1.3: (a) Picture of the NAUTILUS 2260kg ton resonant bar detector currently located at Frascati Laboratories in Rome. (b) AURIGA 2230kg ton resonant bar detector located at Laboratori Nazionali di Legnaro in Padua [6].

Figure 1.4 shows the power spectral density (PSD) collected experimentally from the AURIGA detector compared to the theoretical contribution of noise sources with the sum of all noise shown in black. Thermal noise sources are shown in magenta and light blue, force noise generated by the amplifier is in yellow, and readout noise in green. The dominance of thermal noise demonstrates how important reduction of thermal noise would be for this type of detector, and how they were limited by it.

The strain sensitivity that is expected to be needed to detect binary merger events at least once per year is on the order of 10^{-21} (the target of resonant bar detectors). This combined with their extremely narrow frequency band it is perhaps unsurprising that resonant bar detectors have not yet made any detection of gravitational waves given the magnitude of the noise shown in figure 1.4. As will be discussed in the next section, the sensitivity of km-scale interferometers had improved to the point where in 2003 they exceeded the sensitivity of any existing resonant bar detectors. Interferometer detectors are also sensitive over a much broader range of frequencies, as opposed to resonant bar detectors optimized for one specific resonant mode, allowing interferometers to explore the evolution of a gravitational wave signal in a way that resonant bars cannot. This has led to the replacement of resonant bar detectors by interferometers as the state of the art facilities for gravitational wave detection.

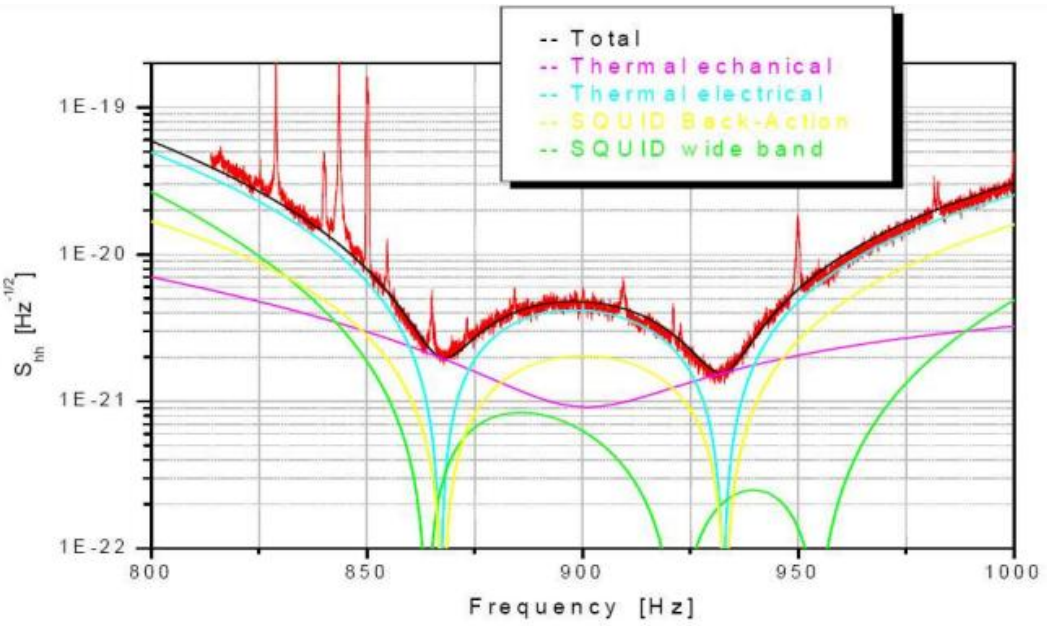

Figure 1.4: Power spectral density of the AURIGA detector operating at 4.5K using a two stage low noise dc-SQUID amplifier. The black line represents a sum of the other predicted noise sources, and the red line is the measured PSD. The dominant noise source is the electrical resonator thermal noise (light blue) except as resonances where antenna thermal noise dominates [6].

Interferometers

The current highest sensitivity gravitational wave detectors are based on the Michelson interferometer design. The Michelson interferometer was developed as part of the famous Michelson-Morley experiment in 1887, which had been designed to show the non-existence of the ether, and it is an instrument that is highly useful for applications where high precision measurement of the difference in the travel times of light traveling along perpendicular directions is important. The basic concept is that a monochromatic light source, typically a laser in modern interferometers, travels through a semi-transparent mirror (called a beam splitter), after which each of the two emerging beams travel down one of two orthogonal "arms" of the interferometer, before reflecting off of a mirror at the end of each arm, returning, and recombining at the beam splitter. Changes in the path length difference change the interference pattern of the two beams.

Tiny variations in the path length difference will result in large changes in the intensity of returning laser as the intensity depends on how the two returning beams interfere with each other.

In gravitational wave interferometry the mirrors at the end of each arm act as test masses that are suspended from pendulums.

In gravitational wave interferometry the mirrors suspended by a system of pendulums, behave as free masses for gravitational waves above the pendulums' resonant frequencies. By using laser interferometry very small variations in the differential displacement of the mirrors can be measured. In theory, displacement of the mirror caused by a passing gravitational wave will result in a path length difference for the laser traveling down each arm. This can be measured as a difference in the intensity of the beam emerging from the beam splitter. In practice, this is exceedingly difficult to accomplish with a simple Michelson interferometer because of engineering constraints and sources of noise that can drown out a gravitational

wave signal.

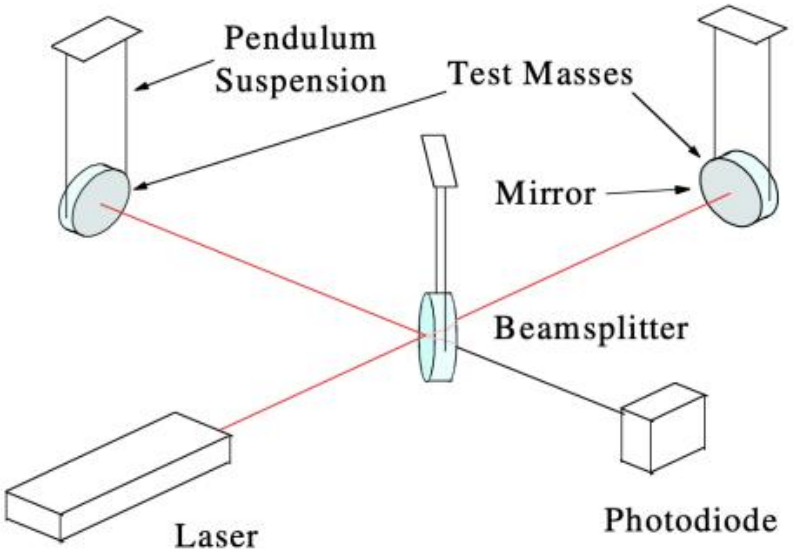

Figure 1.5: This figure shows the configuration of a simple gravitational wave Michelson interferometer.

A gravitational wave passing perpendicular to the plane of detector induces the maximum possible strain, as discussed in section 1.1. The effect of strain on the detector is also maximized in the case that the wave polarization is aligned with the axes of the interferometer, as can be understood from figure 1.1. This variation in length gives the strain measurement $h = \Delta L/L$, where ΔL is the difference in the path length between the two different arms of the interferometer. This variation in path length results in a variation in the intensity of the interferometer output. Since for gravitational waves to be detectable on Earth one would expect h to be on the order of 10^{-21}, it should be obvious why the large length of interferometers is desirable for the detection of gravitational waves.

The laser's electromagnetic field at the input of a Michelson interferometer can be written as [3]:

$$\vec{E_{in}}(x) = E_0 e^{i(\vec{k_L}\cdot\vec{x}-\omega_L t)} \tag{1.12}$$

Here E_0 is the input amplitude of the laser, $k_L = \omega_L/c = 2\pi/\lambda_L$ is the wavenumber of the laser, with ω_L being the frequency of the laser and λ_L being the wavelength of the laser. The laser is then sent to a 50:50 beam splitter and divided into beams E_1 and E_2. These two beams then travel down each arm, reflect off of each mirror, and return to the beam splitter; at which point they can be described as:

$$E_1 = -\frac{1}{\sqrt{2}} E_0 e^{i(2k_L L_1-\omega_L t)} \tag{1.13}$$

$$E_2 = +\frac{1}{\sqrt{2}} E_0 e^{i(2k_L L_2-\omega_L t)} \tag{1.14}$$

Here, $e^{i2k_L L}$ represents the phase difference from the beams that propagate down either arm, with ω_L and k_L being the wavelength and wave number of the laser, respectively. The difference in signs between the two fields is due to the fact that when reflecting off a surface with a high index of refraction a phase shift of π radians is acquired. While traveling through

the beam splitter one of the beams experiences an extra low to high index of refraction reflection and so acquires an extra phase shift of π compared to the other beam, leading to opposite signs. E_1 and E_2 are then recombined in the beam splitter. The combined beam is then redirected to a photodectector. The intensity read by the photodetector is represented by $I_{out} \propto |E_{out}|^2$:

$$|E_{out}|^2 = |E_1 + E_2|^2 = E_0^2 sin^2[k_L(L_y - L_x)] \tag{1.15}$$

In an ideal detector, it is assumed that L_1 and L_2 are equal, and the difference, ΔL, is only induced by the distortion from gravitational waves. So now $k_L(L_y - L_x) = k_L \Delta L$, where $2k_L \Delta L = \Delta\phi$. This shows how any variation in the length of the arms, including from variation induced by a passing gravitational wave, would result in a change in phase at interferometric output.

Here we take the simple case of a gravitational wave propagating along the z-axis perpendicular to the interferometer, with the plus-polarization aligned with the detector arms (or the x and y axes). The effect on the interferometric output can be found, through more complex general relativistic calculations done in [3], to be:

$$\Delta\phi(t) = h_0 \frac{\omega_L L}{c} sinc(\omega_{gw} L/c) cos(\omega_{gw}(t - L/c)) \tag{1.16}$$

Here, L is the length of an arm of the interferometer, ω_{gw} is the frequency of the passing gravitational wave, and h_0 is the amplitude of the gravitational wave. The sinc function is $sinc(x) = sin(x)/x$. In this simple case, the cross-polarization creates no change of phase in the detector, as the effect on both arms would be identical.

Equation 1.16 shows that to get $\Delta\phi$ as large as possible, the length of the interferometer can be optimized. The dependence on L is given by $\frac{\omega_L L}{c} sinc(\omega_{gw} L/c) = \frac{\omega_L}{\omega_{gw}} sin(\omega_{gw} L/c)$. This means that the arm length of the interferometer is optimized by $\omega_{gw} L/c = \pi/2$, or $L = \lambda_{gw}/4$. This yields:

$$L \simeq 750km \left(\frac{100Hz}{f_{gw}}\right) \tag{1.17}$$

This would imply that the optimal arm length for detection would be on the order of hundreds of km. This is clearly infeasible for Earth-based detectors from an engineering and financial standpoint.

At the time of writing, there exist four gravitational wave interferometers on Earth operating in a global network. These are two LIGO interferometers (located in Livingston and Hanford, USA) with arm lengths of 4km, the VIRGO interferometer (near Pisa, Italy), and the KAGRA interferometer (in Hida, Japan), both with arm lengths of 3km. Photos (or a diagram in the case of KAGRA) of these interferometers are shown in figure 1.6.

The interferometer arm length of these four detectors of 3-4km is significantly less than the optimal length of hundreds of kilograms for the detection of binary mergers. However, this optimal distance does not refer to the physical length of the arm, it instead refers to the path length of the light. Two main solutions have been proposed to this problem; delay lines, and resonant cavities.

In the case of delay lines the path length of the laser is extended by reflecting it along non-superimposing paths until the path has reached the desired length. Since the target path length is $\sim$ 750km, and the length of the interferometers currently constructed is 3-4km, the laser would have to bounce on the order of 100 times.

(a) LIGO interferometer located in Livingston, Louisiana, USA

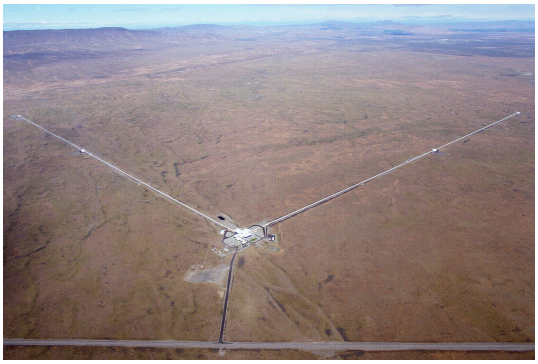

(b) LIGO interferometer located in Hanford, Washington, USA

(c) Virgo interferometer located in Cascina, Pisa, Italy

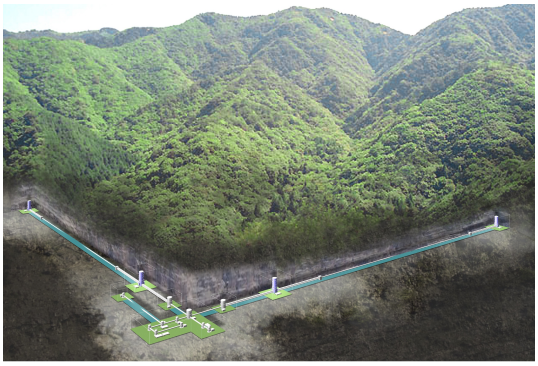

(d) KAGRA interferometer located (underground) in Hida, Gifu Prefecture, Japan

Figure 1.6: Photos (and composite photo/diagram in (d)) of the four currently active gravitational wave interferometer observatories.

The second method of extending the laser path length is by adding a mirror right after the beam splitter on each arm that together with the end mirror forms an optical cavity known as a Fabry-Pérot resonator/cavity. The reflectivities of these mirrors can be chosen to be such that the average path length of a photon inside the cavity is the $\sim$ 750km desired. An example of both methods of extending the path length can be seen in figure 1.7.

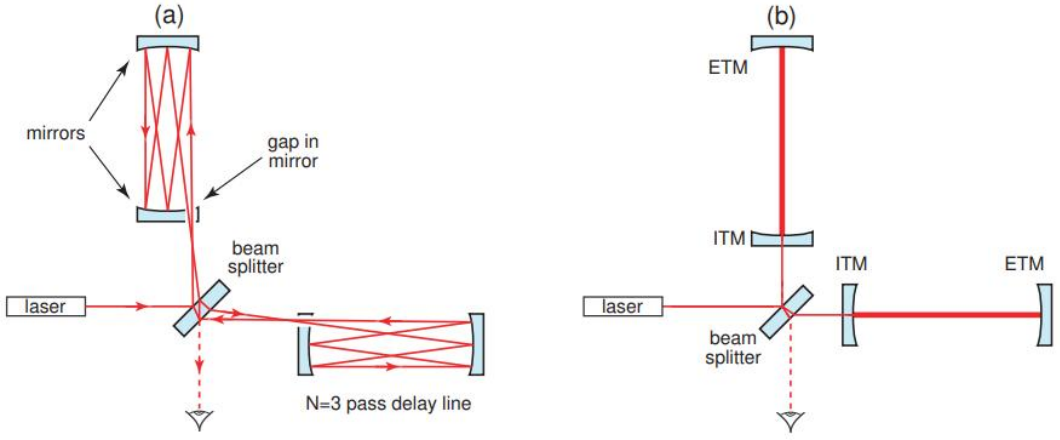

Figure 1.7: Michelson interferometer with (a) delay lines and (b) Fabry-Pérot cavities in the arms to extend the laser path length.

Adding Fabry-Pérot cavities to each arm also has the side effect of increasing the amount of power present in each arm. This same behavior can be taken advantage of to increase the amount of power in the arms by reflecting the power that would return to the laser back into the interferometer. This increase in power increases the sensitivity of the detector through the reduction of shot noise, further discussed in section 1.3. The layout of an interferometer can be seen in figure 1.8.

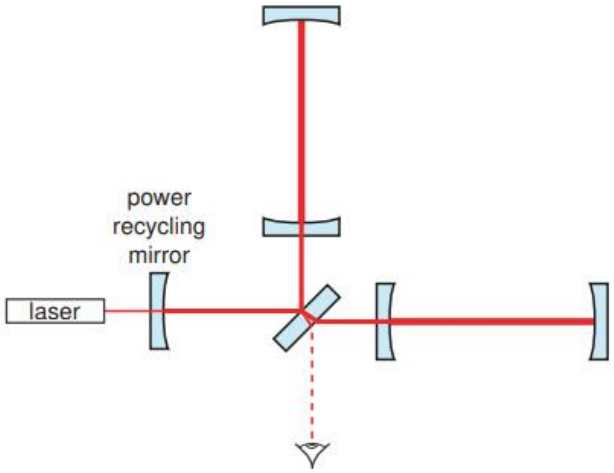

Figure 1.8: Michelson interferometer with Fabry-Pérot cavities and power recycling.

Other advanced techniques are used in gravitational wave detectors that further improve the sensitivity such as input and output-mode cleaners, which are used to reject higher order modes of the laser, signal recycling, and squeezing.

1.3 Noise in Interferometric Measurement

Gravitational wave detectors require high sensitivity in order to measure the very marginal strain induced by gravitational waves. In the case of kilometer-scale interferometers it is necessary to detect displacement of the order of 10^{-18} m. As a result, it is easy for various sources of noise to completely drown out gravitational wave signals. Understanding the noise budget of gravitational wave detectors (as can be seen for the case of the Advanced Virgo detector in figure 1.9) is of the utmost importance for understanding the detector's performance, improving it and eventually improving the signal to noise ratio of detections. In this section some of the main sources of noise in ground based interferometers are outlined.

Seismic Noise

Seismic noise refers to the natural vibrations and movements of the Earth. At reasonably quiet sites on Earth, the level of seismic noise is around $10^{-7}mf^{-2}/Hz^{-1/2}$ in regimes of around 1Hz, with a lower magnitude effect at higher frequencies. Seismic noise can produce effects on interferometers more than 10^{10} times larger than the effects of gravitational waves that would typically be detected.

There are two ways to combat seismic noise, passively and actively. Passive systems including selection of a site with low seismic noise, and passive mechanical filters to isolate sensitive components from the Earth. Pendulums can be used in series to isolate from ground noise from horizontal motion as the response of the pendulum drops as $1/f^2$ above the resonance of the pendulum

Active systems of reducing seismic noise involves using sensors that actively monitor ground motion in order to use actuators to counteract ground motion.

One final technique for circumventing seismic noise, in particular for future detectors where the target gravitational waves are of low frequency and seismic noise would be one of the largest contributors to the noise budget, is to build the detector in space. This is one of the advantages of the future LISA interferometer which aims to detect gravitational waves in a range around $10^{-4} - 10^{-1}$ Hz [8].

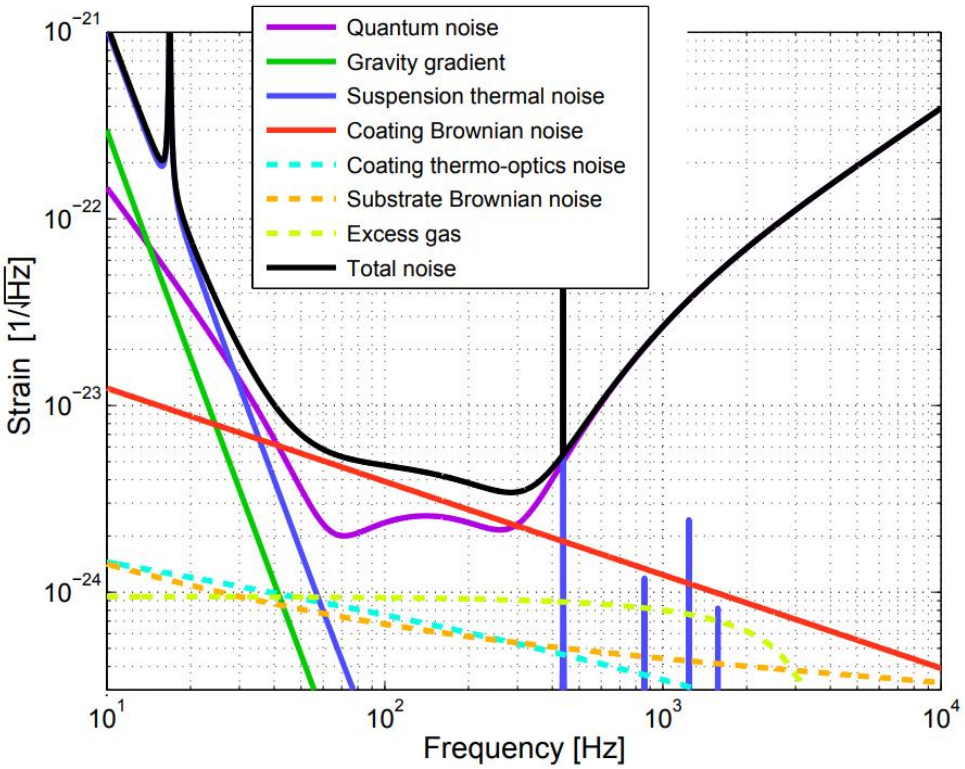

Figure 1.9: Sensitivity curve for the Advanced Virgo interferometer. The overall noise (in black) and different noise sources are shown in terms of the equivalent to the gravitational wave signal would produce at the detector. Figure from [9].

Newtonian Noise

Newtonian noise is noise from changes in the Earth's gravitational field around a detector. It is caused by fluctuations of gravity gradients which impose a differential acceleration on the test masses, mimicking a gravitational wave signal; these fluctuations can be stochastic in nature (from atmospheric effects primarily), or can be of a sinusoidal nature (from seismic waves propagating through the Earth). Though with many sources being distributed in every direction with random frequencies and phases these sinusoidal waves also are functionally stochastic. Studies done on this topic suggest that the dominant source of gravity gradients is seismic surface waves [10]. As Newtonian noise is gravitational in nature, it cannot be shielded either in theory as there is no known way to shield from gravitational effects, or in practice, as it would necessarily also block gravitational wave signals.

Newtonian noise can be passively reduced by building the detector underground. Seismic surface waves and atmospheric effects have less effect on the detector by building underground, away from both sources of noise. Alternatively, the detector can be constructed in space so as to completely avoid the atmosphere and seismic waves [8].

In the future detectors may be able to correct for Newtonian noise using atmospheric and seismic monitoring stations to actively measure the effects that produce Newtonian noise. Using models that explain how these physical effects produce noise, this noise can be removed by subtraction from the output signal of the detector.

Quantum Noise

Quantum noise arises from the discrete quantum nature of light, and can is composed of two separate effects: shot noise, and radiation pressure noise.

The first effect, shot noise, comes from fluctuations of the laser light arriving at the photodetector. The photons arriving at the detector happen as discrete independent events. The distribution of photons arriving at the detector follows Poisson statistics. It can be shown that the detectable strain on the detector is limited by shot noise such that [1]:

$$Strain(Hz)^{-1/2} = \frac{1}{L}\left[\frac{\lambda hc}{\pi^2 P}\right]^{1/2} \tag{1.18}$$

is the limit to the sensitivity imposed by the shot noise. Here λ is the laser wavelength and P is the laser power, h is Planck's constant, and L is the arm length of the detector. This approximation is only valid when the frequency of the laser is below the pole, the frequency of the peak response of the transfer function of the Fabry-Pérot cavity, or there there is no Fabry-Pérot cavity present. One of the key things shown by this equation is that increasing the power of the laser will decrease the shot noise.

The second component to quantum noise is radiation pressure noise. This is a result of photons bouncing off of the test masses at random times, resulting in a stochastic force on the test masses referred to as quantum radiation pressure noise. The displacement of the mirrors/test masses can be described as [1]:

$$\delta x^2(\omega) = N_{ref}^2\left(\frac{4Ph}{M^2\omega^4 c\lambda}\right) \tag{1.19}$$

where P is again the laser power, ω is the angular frequency of the target gravitational wave, M is the mirror mass, c is the speed of light, and N_{ref} is the number of reflections inside a Fabry-Pérot cavity. It should be noted here that while shot noise decreased with laser power, radiation pressure noise increases with laser power. The two of these terms when summed together give the total quantum noise, and the optimum laser power for reducing noise is achieved when these two components of the noise are equal. This means that at each specific frequency there is a fundamental limit to how far quantum noise can be reduced for a simple interferometer setup known at the standard quantum limit; the curve of this optimum quantum noise level is described by [3]:

$$S_{SQL}^{1/2}(f) = \frac{1}{2\pi f L}\sqrt{\frac{8\hbar}{M}} \tag{1.20}$$

where f is the gravitational wave frequency. This standard quantum limit is, in effect, a result of the Heisenberg Uncertainty Principle when formulated for position and momentum [1].

Interferometers can be designed such that the frequency where quantum noise is the lowest is around the frequency range gravitational waves are expected to be detected at. The laser power can be adjusted so that quantum noise is optimized to be as low as possible.

However, it has been demonstrated in the LIGO and Virgo interferometers that it is possible to beat the SQL [11] [12]. This was initially suggested to be possible in the 1980's by introducing quantum correlations by changing the balance between the shot noise and

radiation pressure [13]. In LIGO and Virgo this was achieved through the introduction of a non-classical state of light referred to as squeezed vacuum state, allowing the breaking of the standard quantum limit in certain frequency bands.

Thermal Noise

Thermal (or Brownian) noise is one of the largest sources of noise in current generation gravitational wave detectors for frequencies up to around 300Hz. It is caused by the thermal kinetic energy of the atoms in detectors, with mirror coatings and suspensions being some of the largest contributors. Here we discuss thermal noise with respect to work with bar detectors, but the same key principles apply to the mirrors in interferometers.

It would be reasonable to assume that the minimum detectable energy when dealing with thermal noise would be $\Delta E_{min} \simeq k_B T$, as this is the magnitude of thermal energy that is responsible for thermal fluctuations, however, this is not the case. In his work on early resonant bar detectors, Joseph Weber realized that in a mechanical oscillator with a high Q, the minimum detectable energy would be lower. This is fundamentally due to the fact that in a high-Q oscillator the amount of time it takes to develop energy fluctuations and the amount of time it takes for the bar to return to the ground state after being excited are considerably larger than for a bar with a low Q. Since the duration of a gravitational wave burst τ_g is significantly shorter than the relaxation time of a high-Q material, such as a resonant bar τ_0, the fluctuations due to thermal noise can be expected to be much lower than $k_b T$.

To understand this physical explanation mathematically, the evolution of the fundamental mode of a bar can be studied in the presence of thermal noise. The evolution of the displacement ξ of the bar can be studied by treating it as a damped oscillator:

$$\ddot{\xi} + \omega^2 \xi = -\gamma \dot{\xi} \tag{1.21}$$

where ω_0 is the frequency of the fundamental mode, and γ is the dissipation coefficient. The thermal noise manifests as a stochastic force that scales with the damping factor so that equation 1.21 can be rewritten as [3]:

$$m(\ddot{\xi} + \omega^2 \xi) = F_{therm} = -m_0 \gamma \dot{\xi}_0 + F(t) \tag{1.22}$$

where m is the oscillator mass and where $F(t)$ is the stochastic force that describes thermal fluctuations, which is called the Nyquist force. The thermal fluctuations that cause this force can be described as a stochastic Gaussian process, as they are the sum of many independent contributions. The stochastic force is taken to have an average of 0 and be delta correlated in time. On any macroscopic timescale the autocorrelation of the force can be written as a Dirac delta function.

The fluctuation-dissipation theorem (FDT) allows us to find the PSD of a stochastic process [14]. Using this, the single-sided spectral density $S_{F_{therm}}$ of the stochastic force F_{therm} in equation 1.22 can be found as a function of the dissipative term:

$$S_{F_{thermal}}(\omega) = 4 k_B T \gamma \tag{1.23}$$

where k_B is the Boltzmann constant and T is the equilibrium temperature. This result represents a specific case of the fluctuation-dissipation theorem, which can then be formulated to describe a linear mechanical system $x(t)$ subjected to an external force $F(t)$, where $\dot{x}(t) = v(t)$. First we can express this general linear system in Fourier space:

$$\tilde{F}(\omega) = Z(\omega) v(\omega) \tag{1.24}$$

where $Z(\omega)$ is the impedance of the system. The FDT tells us that the single-sided power spectrum of the stochastic force of thermal origin driving the system can be related to the real part of the impedance $R(\omega)$ as:

$$S_F(\omega) = 4k_BTRe(Z(\omega)) = 4k_BTR(\omega) \tag{1.25}$$

It is useful now to revisit a similar formulation for the motion of the damped oscillator as we had in equation 1.21. Here, the motion of the particle is subject to velocity damping, a simple Hooke oscillator restoring force, and to the thermal noise [15]:

$$m\ddot{x}(t) + \gamma\dot{x}(t) + kx(t) = F_{th} \tag{1.26}$$

with $\gamma = m\omega_0/Q$ as the damping coefficient and $k = m\omega_0^2$ as the spring constant of the Hooke restoring force. We can use this formulation of the force to find the real part of the impedance $R(\omega)$ as impedance is defined as $Z \equiv F/v$:

$$R_{damped}(\omega) = Re\left[\frac{F}{\dot{x}}\right] = Re\left[\frac{m\ddot{x}(t) + \gamma\dot{x}(t) + kx(t)}{\dot{x}}\right] = Re\left[i\omega m + \gamma + \frac{k}{i\omega}\right] = \gamma \tag{1.27}$$

By inserting the value of $R(\omega)$ into equation 1.25, we recover the same spectrum of thermal noise found in equation 1.23. We find that the driving stochastic force has a PSD that is constant in frequency using this model of the damped oscillator.

We can express equation 1.26 in the frequency domain by performing a Fourier transform. The power spectral density of the particle motion $S_x(\omega)$ induced by thermal noise can now be expressed as:

$$x(\omega) = \frac{4k_BT\gamma}{-m\omega^2 + i\omega\gamma + k} = H(\omega)F_{thermal}(\omega) \tag{1.28}$$

where $H(\omega)$ is the transfer function of the thermal noise. This transfer function can then be used to find the power spectral density of the position of the oscillating mass:

$$S_x(\omega) = |H(\omega)|^2 S_{F_{th}}(\omega) = \frac{4k_BT\gamma}{(k - m\omega^2)^2 + (\omega\gamma)^2} = \frac{4k_BT}{mQ\omega_0}\frac{1}{\left(1 - \frac{\omega^2}{\omega_0^2}\right)^2 + \left(\frac{\omega}{Q}\right)^2} \tag{1.29}$$

where $S_{F_{th}}$ is the power spectral density of the stochastic force of the thermal noise that drives the fluctuations, and ω_0 is the resonant frequency.

With high sensitivity experiments, the relevant loss mechanism is often not due to viscous damping but to internal damping. In the case of internal damping in materials an extension of Hooke's law can be used [16]:

$$F_{ID} = -k[1 + i\phi(\omega)]x \tag{1.30}$$

For a sinusoidal force, the mass moves with a time lag with respect to the driving force offet by the angle $\phi(\omega)$. A fraction of the energy stored in the oscillatory motion ($2\pi\phi(\omega)$) is dissipated each cycle, resulting in damping [15]. Taking internal damping into account, the power spectral density of the internal driving force can be expressed as:

$$S_{F_{th},ID}(\omega) = 4k_BTk\phi(\omega)\omega^{-1} \tag{1.31}$$

In equation 1.27 we found that the noise was white in nature in the case of velocity damping, this is no longer the case with internal damping. The power spectral density of the position of this internally damped oscillator can now be expressed as:

$$S_{x,ID}(\omega) = |H(\omega)|^2 S_{F_{th},ID}(\omega) = \frac{4k_BTk\phi(\omega)}{\omega[(k-m\omega^2)^2 + (k\phi(\omega))^2]} = \frac{4k_BT}{\omega\omega_0^2 mQ} \frac{1}{\left(1-\frac{\omega^2}{\omega_0^2}\right) + \left(\frac{1}{Q}\right)^2} \tag{1.32}$$

where the internal damping quality factor is $Q = 1/\phi(\omega)$. The quality factor Q also defines the sharpness of the resonant peak in the power spectral density of the position, since the quality factor is defined as $Q = \omega_0/\Delta\omega$, where $\Delta\omega$ is the full width at half maximum of the peak. For these high Q systems, the power spectral density will have a sharp peak around the resonant frequency.

The fluctuation-dissipation theorem already discussed is used to describe thermal noise in thermodynamic equilibrium. As discussed earlier in this chapter, different types of damping will result in different thermal noise behaviors, as can be seen in the spectral density responses of different systems in figure 1.10.

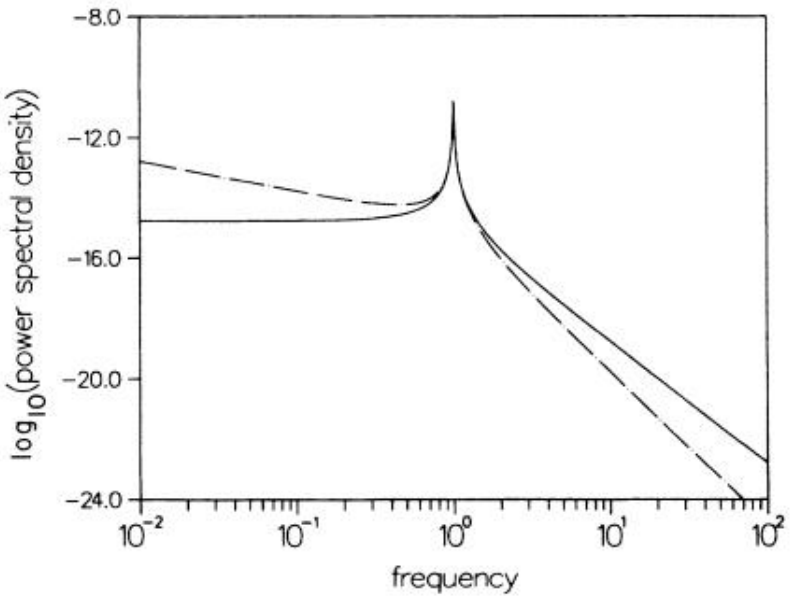

Figure 1.10: Power spectral density of thermal noise for two differently damped mechanical oscillators. For both oscillators $m = 1$g, $\omega_0 = 1$ s^{-1}, and $Q = 100$. The solid line represents an oscillator that is experiencing velocity damping and the dashed line represents an internally damped oscillator.

We can now integrate equation 1.28 over all frequencies, resulting in the mean-square displacement of the particle of:

$$\bar{x}_{th}^2 = \frac{k_BT}{k} \tag{1.33}$$

Which can also be expressed as:

$$\bar{x}_{th}^2 = \frac{k_BT}{m\omega_0^2} \tag{1.34}$$

This is consistent with the equipartition theorem, which states that each quadratic term in the energy has a mean value of $\frac{1}{2}k_BT$.

1.4 Non-Equilibrium Thermal Noise

Thermal noise is one of the largest contributors to the noise budget of current-generation gravitational detectors, with it being the largest contributor at some frequencies. Thermal noise in detectors is currently modeled using the FDT, which is well experimentally confirmed to be able to model thermal noise in thermodynamic equilibrium, but not for systems out of thermodynamic equilibrium. Modeling gravitational wave detectors as systems in thermodynamic equilibrium is not likely to be accurate. In interferometers, many processes, such as the dissipation of laser thermal energy in the suspension fibers, thermal compensation for thermal lensing effects in the mirrors, the future addition of cryogenic systems to interferometers are expected to drive the system out of thermodynamic equilibrium.

Since detectors cannot be considered systems in thermodynamic equilibrium, and the FDT is insufficient to model systems out of thermodynamic equilibrium, a new theory is needed to fully model noise in these non-equilibrium steady states. As a result, there has been increased interest in understanding thermal noise out of thermodynamic equilibrium.

Historically, experiments on thermal noise out of thermodynamic equilibrium have been done at very small scale due to the difficulty of measuring thermal noise in macroscopic systems. In this section, there is a brief discussion of one of the microscopic projects involving a micro-cantilever heated by a laser [17] and a discussion of one of the few macroscopic experiments, RareNoise [18].

Micro-Cantilever Thermal Noise Experiment

In Geitner et al. 2017 [17], the behavior of noise in a non-equilibrium steady state (NESS) was studied in a small-scale cantilever (with a length of 500 µm). The end of the cantilever was heated from partial absorption of laser light, which made up one of the two beams in a differential interferometer, as can be seen in figure 1.11. The second beam reflects off of the clamp that holds the cantilever in place.

Sharp resonances can be seen in the power spectral density of the displacement of the cantilever arm, as seen in figure 1.12, which are assumed to be driven by the thermal noise. Using cantilever arms with very high quality factors allows the peaks to be modeled as independent harmonic oscillators.

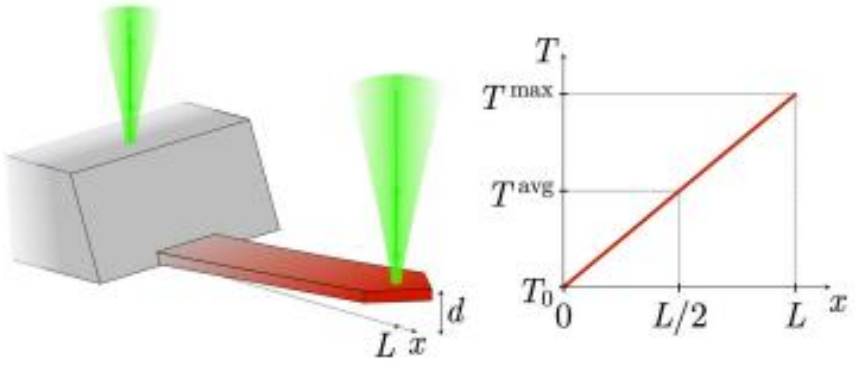

Figure 1.11: Experimental setup of micro-cantilever experiment. The deflection d of the cantilever is measured using the interference of two lasers which are reflected off of the cantilever arm and the clamp holding the cantilever. The beam heats the sensing arm and the heat propagates along the arm giving the heating profile shown on the right, where T grows linearly along x, coordinate axis of the cantilever length L. The system is heated to reach a non-equilibrium steady state.

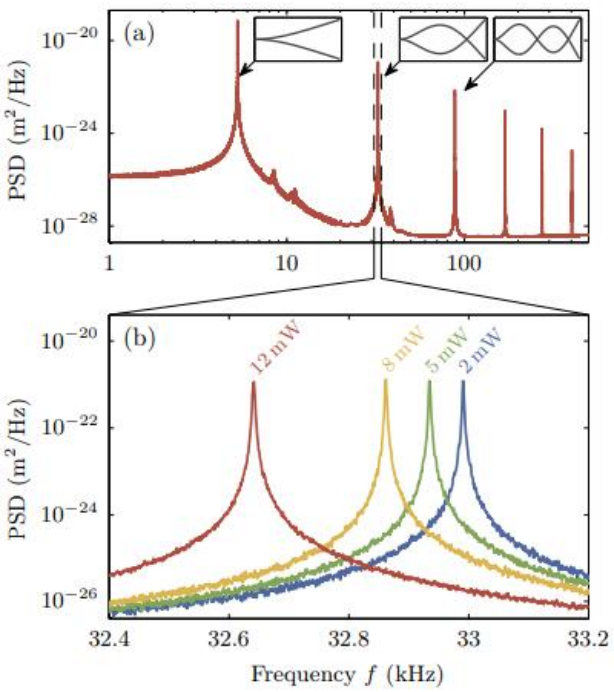

Figure 1.12: Power spectral density of the thermal noise induced deflection as a function of frequency. (a) Each of the sharp peaks corresponds to a resonant mode; these resonances can be modeled as simple harmonic oscillators. The area under the PSD peak gives the mean square deflection of each degree of freedom, and can be used to find their effective temperatures. (b) This figure shows a zoom in on one of the resonant modes. With increasing laser power, and so average temperature of the cantilever, the resonant frequency can be observed to decrease due to the softening of the cantilever. The frequency is used to estimate and track the temperature profile and the average temperature. Figure from [17].

The work starts from a generalization of the FDT and demonstrates that this assumption can lead to apparent deficits of thermal noise in specific cases.

In order to quantify the amplitude of thermal fluctuations of each mode n, the authors extended the definition of the equipartition theorem, formulated previously as equation 1.34, in order to define the effective temperature T_n^{eff} such that:

$$\frac{1}{2}k_n\langle d_n^2\rangle = \frac{1}{2}k_B T_n^{eff} \tag{1.35}$$

where k_n is the stiffness of the mode, $\langle d_n^2\rangle$ is the mean square displacement of the mode n, and k_B is the Boltzmann constant.

The effective temperature of each mode can be found from the PSD of the displacement, as seen in figure 1.12. The average temperature and T_n^{eff} were tracked at different laser power levels first for a pure silicon cantilever, and then again for a tantala-coated cantilever. Figure 1.13 shows the results for both cantilevers, T_n^{eff} for each flexural mode, and the average thermodynamic temperatures as a function of the laser power.

The two cantilevers show very different behavior. The pure silicon cantilever shows little variation between different modes, and the measured effective temperatures in fact are closer to the room temperature (295K) than to the average temperatures of the cantilever over the different trials. For the tantala-coated cantilever, the effective temperature shows a clear mode dependence and at least reasonably closely matches the average temperature for the modes $n > 1$. For the silicon cantilever and the first flexural mode of the tantala-coated

cantilever, the trials actually show a deficit of thermal fluctuations compared to what would be expected in equilibrium at the average temperature.

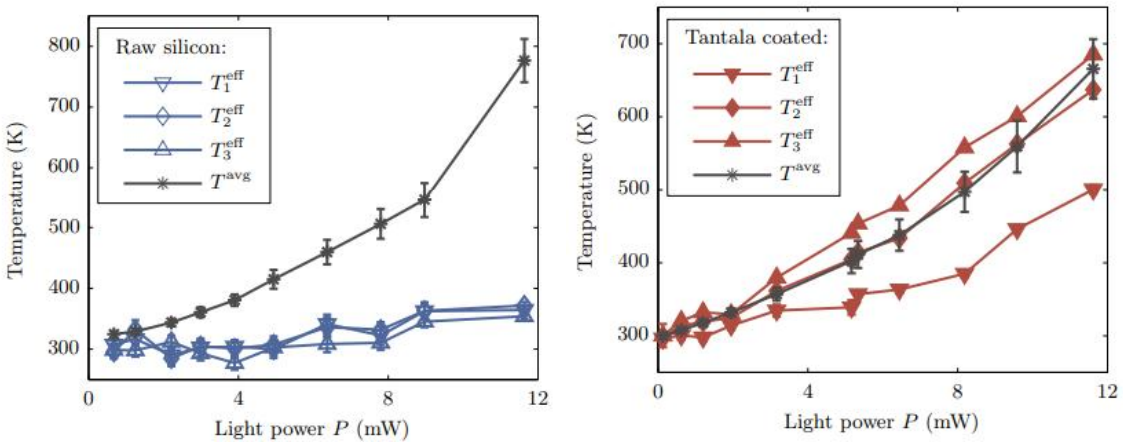

(a) Silicon cantilever trials

(b) Tantala coated cantilever trials

Figure 1.13: Effective temperature for the first three flexural modes, and average temperature for two different cantilevers for different laser power levels. (a) Represents trials done with a raw silicon cantilever, and (b) represents trials done with a tantala-coated canitlever. Figure is from Geitner et al. 2017 [17].

Starting from the FDT generalization, the experiment shows that for a system of the same average temperature as an equilibrium state, a deficit of thermal noise is actually possible in a NESS. This is unexpected and contrary to what other experiments with different experimental setups have been found, as noted in Geitner et al. 2017 [17] and warrants further experimentation with NESS for the study of thermal noise out of thermodynamic equilibrium for macroscopic systems.

The RareNoise Experiment

The RareNoise experiment aimed to study thermal fluctuations in non-equilibrium macroscopic systems, with the specific goal of understanding noise from thermal gradients in gravitational wave interferometers [18]. The experiment investigated the effect of thermal gradients on a mechanical oscillator in a small frequency range around the resonance modes of the oscillator, designed to be in the frequency range of interest for gravitational wave detection. The mechanical oscillator is chosen to be a low-loss one to best reproduce the situation inside gravitational-wave interferometers.

The experiment consists of an oscillator placed inside a vacuum chamber with a series of mechanical filters designed to isolate the oscillator from outside noise sources [19]. The oscillator is composed of a monolithic aluminum piece with a cuboid mass placed at the end of a rod with a square cross-section of 0.1m in length. The oscillator has its first transverse mode at around 320Hz and its first longitudinal mode around 1400Hz; at these frequency ranges the dominant force acting on the oscillator is the thermal noise. Diagrams of the oscillator and its resonant modes of interest can be seen in figure 1.14.

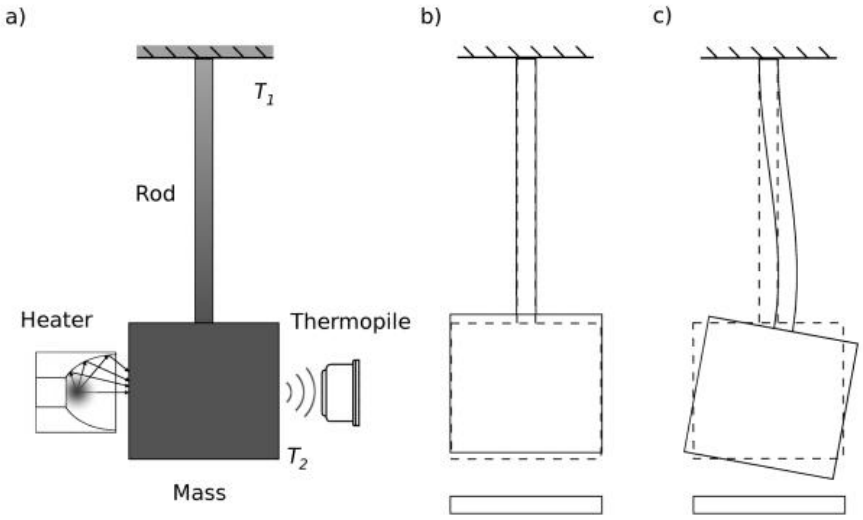

Figure 1.14: Schematic of the resonant oscillator used in the RareNoise experiment, consisting of a rod fixed on one end with a cubic mass free to move on the other. In (a) the IR heater used to establish a NESS and the contactless thermopile used to measure the mass's temperature are both visible. A NTC thermistor is also located on the top of the rod to measure the temperature there, with the thermal gradient of the system indicated in the shading of the figure (darker is higher temperature). The first longitudinal mode is shown in (b) and the first transverse mode is shown in (c). The resonant frequencies for these two modes are expected to be around 1.4kHz and 320Hz respectively. Figure taken from Conti et al. 2013 [19].

An infrared heater is used to drive the oscillator out of equilibrium and establish a NESS. A thermopile and an NTC thermistor are used to measure the temperature of the mass and the top of the oscillator rod, respectively, to measure the temperature difference across the square oscillator rod ΔT.

The full frequency band between 200Hz and 3kHz was free from mechanical noise from both ground noise and internal resonance of the payload. The average PSDs were then fit around each resonance, by a curve resulting from a Lorentzian with a constant continuum of white noise [19]:

$$y(f) = \frac{p_1 p_2}{4(f - p_0)^2 + p_1^2} + p_3 \tag{1.36}$$

where p_0 is the resonant frequency, p_1 is the full width at half maximum (FWHM), p_2 is $2/\pi$ times the area under the Lorentzian curve, and p_3 is the constant representing the noise level out of the resonance peak. Two fitted Lorentzian peaks can be seen in figure 1.15, one representing the experiment carried out in thermodynamic equilibrium, and one for a NESS.

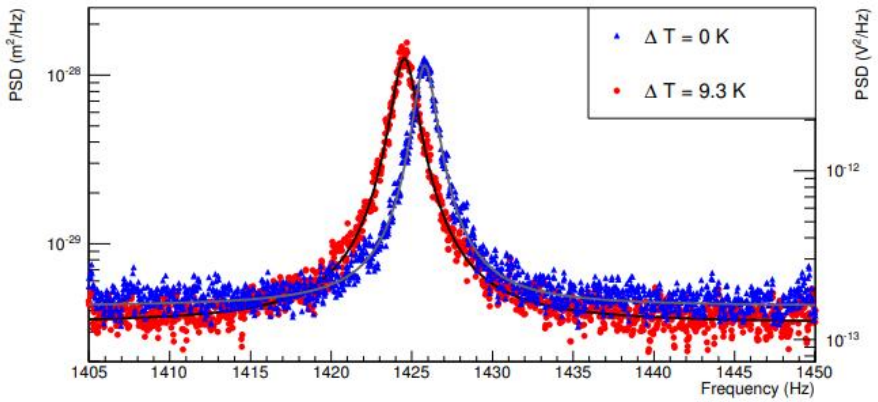

Figure 1.15: Two time averaged PSDs are visible here for the first longitudinal mode in equilibrium (blue triangles, $T_{avg} = 288.14K$) and for a NESS (red circles, $\Delta T = 9.3K$, $T_{avg} = 292K$, where ΔT is the temperature difference between the mass the the top of the oscillator. Each set of data has a fit line shown in gray, for the equilibrium state, and shown in black, for the NESS. Figure is taken from [19].

The area of the Lorentzian fitting curve can be used to estimate the mean square vibration $\langle x(t) \rangle^2$ of the oscillator. As previously shown in equation 1.34, in an equilibrium system with low losses the mean square displacement can be found from the equipartition theorem, as can be seen in equation 1.34.

Before the introduction of NESSs to the experiment, tests were conducted in equilibrium at different equilibrium temperatures to confirm that T_{eff} was a good estimate of thermodynamic temperature here, which was the case.

Once this was confirmed, tests could be run with NESSs, which were characterized by a thermal difference $\Delta T = T_2 - T_1$ and an average temperature $T_{avg} = \frac{T_1+T_2}{2}$ (for the longitudinal mode only) where T_2 is the measured temperature of the oscillator mass and T_1 is the temperature of the top of the oscillator rod. For the transverse mode, T_{avg} was estimated from the shift of the resonant frequency peak.

Now, a ratio $R_{NEQ/EQ} = T_{eff}/T_{eq}$ is introduced, where T_{eq} is the effective temperature at equilibrium, which is plotted against $\Delta T/T_{avg}$ in figure 1.16. $R_{NEQ/EQ} > 1$ for all measurements taken. At the largest relative temperature difference measured $R_{NEQ/EQ}$ is greater than 1 by more than 4 standard deviations for the longitudinal mode. It is shown that a 4% difference in relative temperature is enough to increase the non-equilibrium T_{eff} by 20%, meaning it is higher than any physical temperature in the oscillator [19]. For the transverse mode an even more remarkable departure from the equilibrium case was measured, which demonstrates that T_{eff} is not a valid representation of the thermodynamic temperature away from equilibrium, even if the divergence from equilibrium is small.

A numerical experiment was also conducted for a chain of 1-dimensional oscillators, the results of which are reported in figure 1.16 [19]. The results of the numerical investigation match the experimental results shown in the figure, however these results model a 1D chain and so can only be compared to the longitudinal mode. This experiment not only challenges the validity of T_{eff} as an estimate of the thermodynamic temperature, but also if the equipartition theorem holds in a NESS. The average energy does not match the expected values, which also suggests that the energy is not equipartitioned between different modes, meaning that each would be characterized by a different T_{eff}.

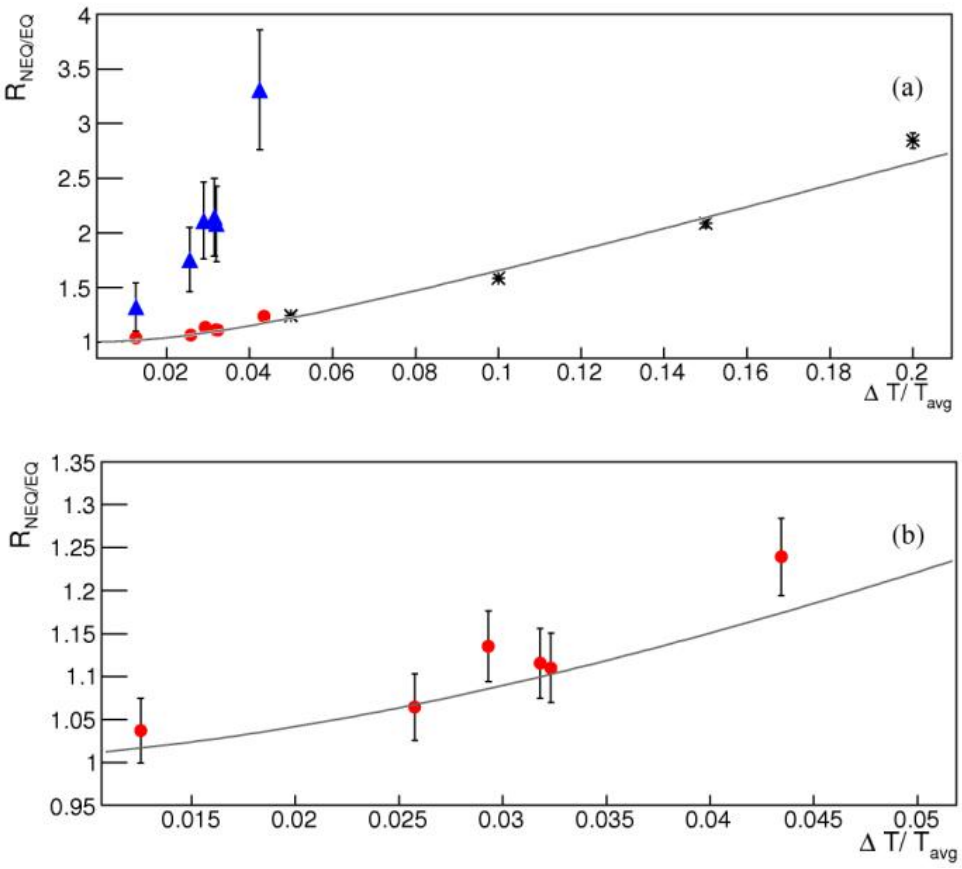

Figure 1.16: The ratio $R_{NEQ/EQ} = T_{eff}/T_{eq}$ vs the normalized thermal difference $\Delta T/T_{avg}$ for the transverse mode (blue triangles) and longitudinal mode (red circles) for the 1-dimensional oscillator numerical experiment done as part of the RareNoise project. Error bars report statistical uncertainty, which are very small along the x-axis. The black stars show the results of the numerical experiment, with the gray line being their line of best fit. The right figure is a zoomed in version of the top figure to show the behavior of the longitudial mode more clearly. Figure taken from [19].

The results of the experiments discussed here show somewhat conflicting results, indicating a need for further study in this area. The Non-Equilibrium Thermal Noise (NETN) experiment aims to reproduce the experimental setup and results of the RareNoise experiment in such a way that experiments can be performed with a larger thermal gradient and with a most robust calibration system. The NETN experiment's use of a quadrature phase differential interferometer in particular allows for higher sensitivity and allows for unambiguous extraction of the phase.

2 Non-Equilibrium Thermal Noise Experimental Setup

In this chapter, the experimental setup of the Non-Equilibrium Thermal Noise (NETN) experiment is discussed. Some of the experimental setup is borrowed from [20] the RareNoise experiment [19] discussed in section 1.4.

2.1 Experimental Setup

Oscillator and Reference Mirror

The vacuum chamber houses an oscillator which is structured as a square rod with a cuboid mass at the end. The oscillator is a single machined piece of AL5056 aluminum alloy which is characterized by low intrinsic mechanical losses. The cube mass is 5cm on each side, with the bottom polished to act as a mirror for the interferometer. The rod is 100mm long with a 5.5mm square cross section. A figure of this system can be seen in 2.1a. The oscillator is mounted vertically with the cube at the bottom, free to oscillate, with the reflective surface at the bottom of the cube.

A piezoelectric actuator is attached to the top of the oscillator which can be used to excite it, in particular, the first longitudinal and transverse resonant modes. The actuator is mounted coaxially with the oscillator. The actuator can be used generally to excite the oscillator, but is primarily used to measure transfer functions of the oscillator's response to excitation of different frequencies in order to precisely locate the value of its resonant modes, as they may shift slightly over time.

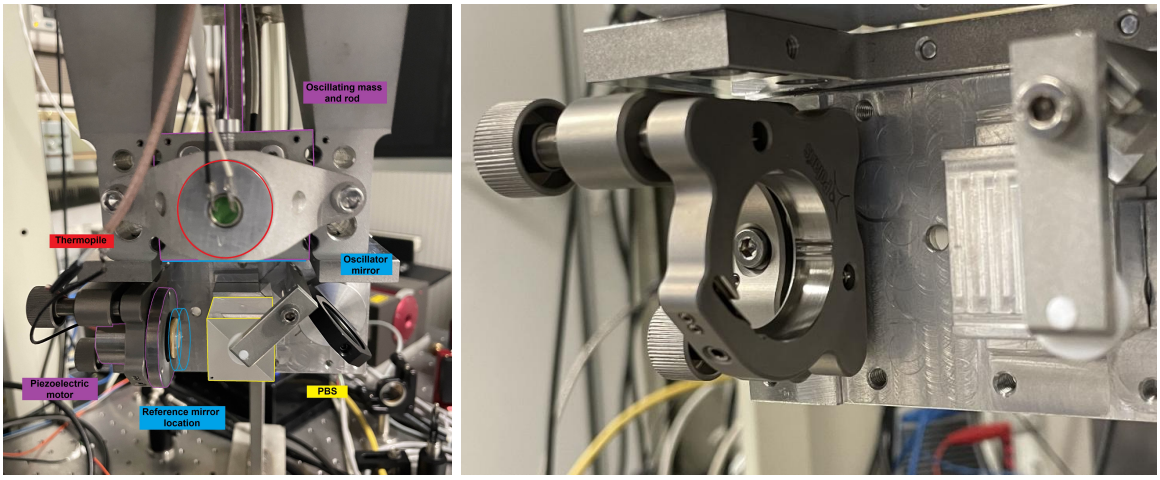

(a) Oscillator and optics inside the chamber

(b) Empty bracket for reference mirror/piezoelectric motor during upgrades

Figure 2.1: The figures here show a labled version of the internal optics for the chamber, showing where to reference mirror was before detaching, as discussed in 4.1.

The first longitudinal mode of the oscillator is typically around 1408Hz at room temperature, which has been observed to shift lower at higher temperature, with it being observed down to around 1401Hz. The first transverse resonant mode is around 300Hz, which has been investigated less precisely due to the fact that it is harder to model, and it falls in a frequency region with higher environmental noise. For the first longitudinal mode, the oscillator can be considered a damped simple harmonic oscillator schematized as a spring-mass system, where the rod acts as a spring and the cuboid as an inertial mass. The thermal noise acts as a stochastic force in this model.

Inside of the vacuum chamber, there is a polarizing beam splitter than separates the beam into two orthogonally polarized beams (as is discussed in more detail in chapter 3), and there are two reflecting surfaces that reflect one of each of the two polarization modes of the laser back out of the chamber. One of the reflecting surfaces is a fixed mirror that is referred to as the reference mirror. At the start of this thesis work the mirror was attached to a piezoelectric actuator, but for reasons that will be discussed in 4.1 the actuator was removed. This mirror is similar to the steering mirrors in the experimental setup in that it has an HR coating matched to the laser wavelength, with the one notable different that the steering mirrors have an angle of incidence of 45 degrees, and the the reference mirror is 0 degrees. The second reflecting surface inside of the vacuum chamber is the bottom of the oscillating mass, whose motion is being investigated in order to isolate the thermal noise contribution.

Laser

The laser used in this experiment is a continuous wave laser with a wavelength of 1064nm. This wavelength matches the wavelength of laser used in current ground-based gravitational interferometry at LIGO, Virgo, and KAGRA. The nominal power of the laser is 500mW but due to aging in practice was generally running well below that. Issues with the laser power decreasing with time are discussed further in section 4.3.

IR Heater and Temperature Measurement

Since a goal of the experiment is to measure thermal noise out of thermodynamic equilibrium, it is necessary to be able to induce a non-equilibrium steady state (NESS) on demand. For this purpose, the experiment contains an IR heater that can be used to heat one side of the oscillator mass. The IR heater consists of a 3.6Ω resistor that emits heat in the form of blackbody radiation as a current is applied. The resistor is at the focal point of a parabolic mirror that allows it to irradiate the oscillator mass. The thermal gradient across the rod is the largest contributor to the NESS.

The temperature of the experiment can be monitored using two devices inside the chamber. An NTC thermistor mounted on the top end of the rod allows for measurement of the temperature of the oscillator base (ref fig 14). A thermopile on the opposite side of the oscillator mass allows for the contactless measurement of its temperature, T2 in figure 1.14. In addition to the temperature measurements inside the chamber, there are two thermometers that measure the temperature on the top of the chamber and the ambient temperature of the room. The thermopile and the thermometer at the top of the rod can be used to measure the thermal gradient across the oscillator rod by way of providing a measurement on either end of it.

Heating Coil

The past work on this experiment only used the IR heater inside the chamber to adjust the temperature. This could introduce a NESS on the system, but a different heating method was needed for the measurement taken during this thesis work. A resistive coil was wrapped around the vacuum chamber to be able to raise the temperature of the entire chamber tens of degrees. This was done for the purpose of being able to create equilibrium states at different temperatures greater than room temperature. A current controlled by a power supply can be run through the coil in order to heat it and the chamber. A layer of insulation was wrapped around the chamber while taking measurements while heating. The highest power which the heater had been run at is around 71W, resulting in a measured chamber temperature of

around 323K, around a +25K increase, but in theory higher temperatures could be achieved where the experiment could be run safely.

Issues that arose during the first attempts to collect data while using the heater are discussed in section 4.1.

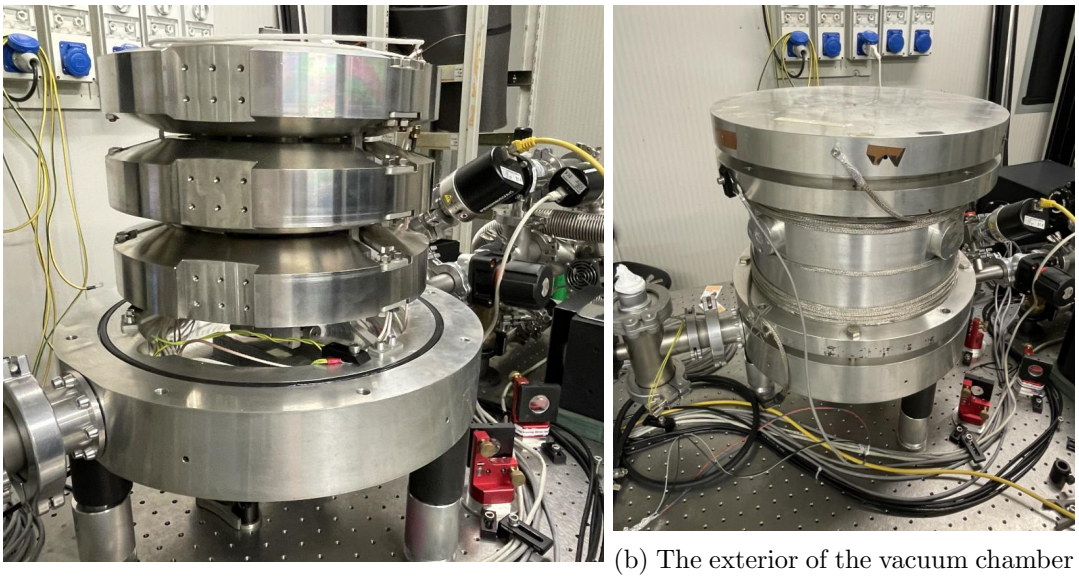

(a) Photo of three mechanical filters inside of the vacuum chamber when it was opened for maintenance.

(b) The exterior of the vacuum chamber with the heating coil used to establish thermodynamic equillibrium at different temperatures

Figure 2.2: Interior and exterior of chamber.

Mechanical Filters

The experimental setup has multiple noise filtering systems to isolate the oscillator from external vibrations. The first stage of noise filtering is that the entire optical bench the experiment is set up on is on an air-suspended table, acting as an initial filter against seismic noise above a few Hz.

The vacuum chamber is on this table, and is supported by three nylon spacers, which in turn are supported by three aluminum cylinders, with a cube of Sylodamp placed in between each set of nylon and aluminum supports, as can be seen in figure 2.3. The nylon spacers were used in the RareNoise previously for thermal insulation. The Sylodamp is a vibration damping elastomer and acts as a second layer of mechanical filtering, after the legs. Sylodamp in particular can damp vibrations in the range of 10-70Hz, and reduces the vibrations in the chamber in both this range.

A piece of Sylodamp is also used to isolate the ion pump from the optical bench due to the ion pump being rigidly connected the the vacuum chamber, which could otherwise introduce noise to the system.

Most of the mechanical filtering in the experimental range of interest (300-2000Hz), the range where the longitudinal and transverse resonance modes of the oscillator lie, comes from the three-stage mechanical filter inside of the vacuum chamber [21]. This mechanical filtering system was designed for the RareNoise experiment to isolate that experiment from mechanical noise while fitting inside of the vacuum chamber. The system has three separate stages, each comprised of a mass and three C-shaped springs that connect it to either the floor of the chamber or the mass below it, with the top mass supporting the bracket that holds the oscillator and some of the experiment's optics, as well as the IR heater and some of

the temperature measuring elements.

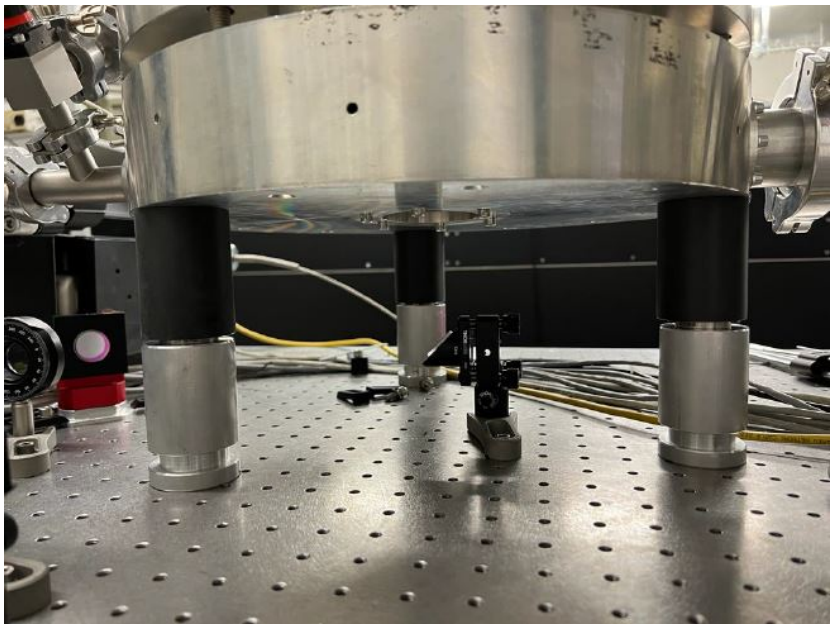

Figure 2.3: Photo of the pillars supporting the vacuum chamber from the previous work done on the experiment [22]. The black part of the pillar is nylon and the silver is aluminum. Each leg has a cube of sylodamp compressed between these two parts to help minimize the external vibration being transmitted to the chamber.

Each mass has a diameter of 305mm and a height of 260mm, with the masses being 17.4, 17.4, and 19.8kg. The top mass is more massive due to supporting the 6.6kg assembly of the oscillator and relevant optics and electronics. Each stage of the filter is a single oscillator that resonates at a frequency well below the first transverse mode of the oscillator in the experiment (∼300Hz).

Equation 2.1 describes the transfer function of the oscillator. This holds in the regime where $f_0^2 << f << f_0/\phi$, with ϕ representing the loss angle of the oscillator representing the mechanical filter. Using this, we chose mechanical filters with a resonant frequency well below that of the region of interest.

$$T(f_0, f) = \frac{f_0^2}{f_0^2 - f^2} \tag{2.1}$$

The filters used for the RareNoise and NETN experiments have a resonant frequency of v_0 ≈38Hz. With the cascade of all three filters, the behavior is much more complex, as can be seen in figure 2.4. The three filter stages greatly reduce noise in frequencies significantly above this 38Hz frequency, including in the range of around 300Hz that the first transverse mode of the oscillator is. The filters were also designed to have the lowest internal resonance of the elements be above 2kHz [21]. This is above the region of interest for this project, with the main frequency of interest being around 1400Hz where the first longitudinal mode of the oscillator is.

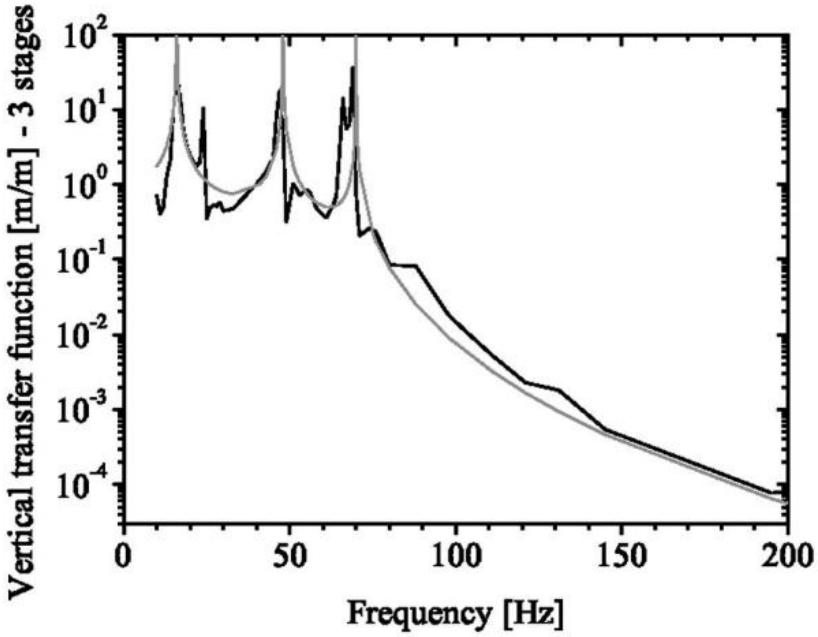

Figure 2.4: Figure shows the vertical transfer function of the full three-stage mechanical filtering system. The filtering system consists of three stages each resonating at 38Hz. The black line represents the experimentally measured response, and the gray line represents the predicted response from coupling all three stages in cascade with the three masses of 17.4, 17.4, and 19.8kg [21].

Data Collection Elements

Two types of data are collected for the experiment. "Fast" data are collected by four photodiodes and are captured at a sampling frequency of 8000Hz at a $\pm$10V range for the purpose of being able to investigate the behavior of the experiment at high frequencies; and "slow" data are captured from diagnostic and environmental sensors at a sampling frequency of 1Hz for the purpose of measuring long term behavior of the experiment.

The data from the four photodiodes of the interferometer are acquired using a 24-bit resolution ADC NI PXI-4462 DAQ board. All of the slow channel environmental inputs (temperature and pressure) are acquired with NI 9219 24-bit universal analog inputs. Temperature acquisition is discussed in greater detail in section 2.1. Pressure is measured by three vacuum gauges placed in different sections of the vacuum chamber and pumping system, as can be seen in figure 2.5.

The layout of the interferometer can be seen in figure 2.6 (with the updated layout shown in chapter 4 in figure 4.6).

Lenses L1, L2, and L3 make up a telescope that collimates the beam, with focal lengths of 100, 150, and 1000mm respectively. The resulting beam has a waist of $\sim$1mm and a Rayleigh range of $\sim$2.95m.

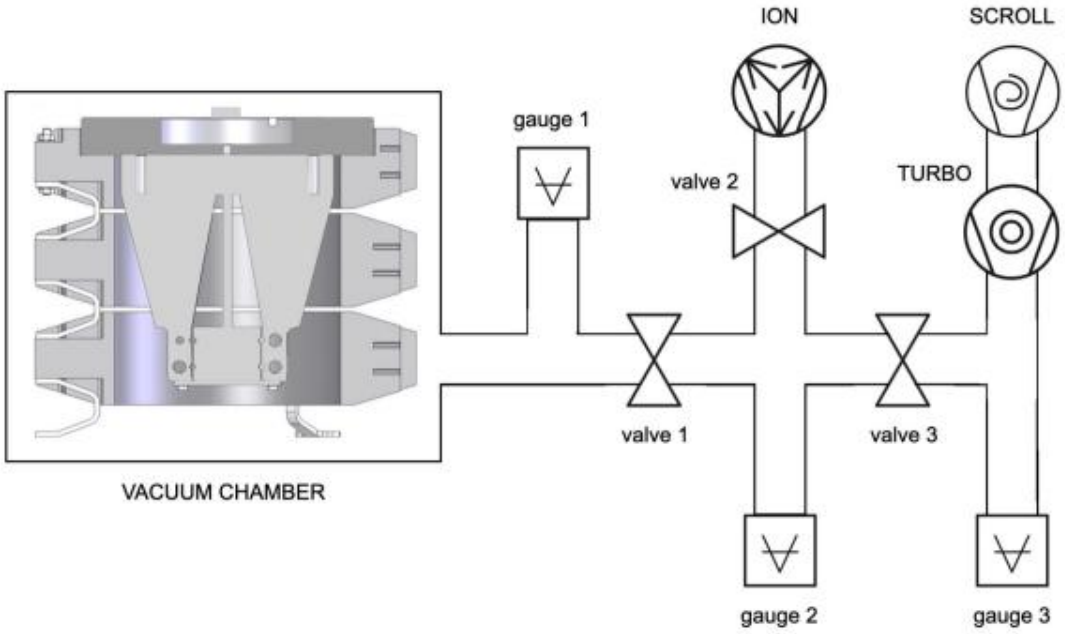

Figure 2.5: Layout of the pumping system for the vacuum chamber. The scroll and turbopump systems are used to hit the target pressure of $\sim 10^{-5}$mbar, after which the ion pump is used on its own to maintain this pressure while minimizing vibration created on the optical bench [20].

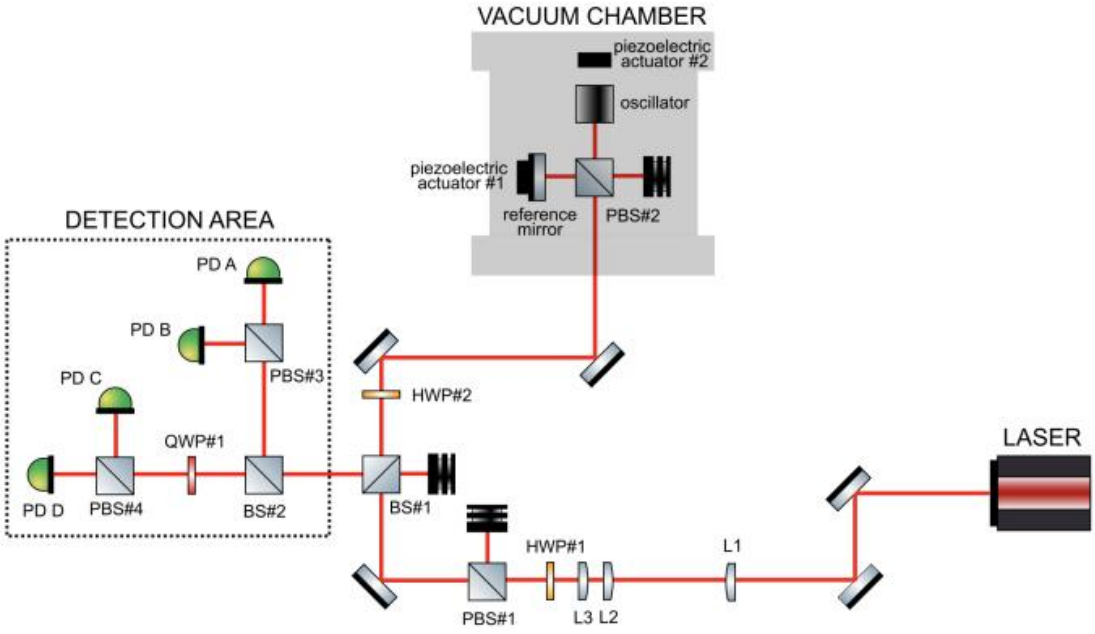

Figure 2.6: Layout of the optics at the start of the thesis work. The detection area is the section of the optical bench containing the four photodiodes. Figure taken from [20].

HWP 1, placed immediately after the telescope, is used in conjunction with PBS 1 to allow the power of the laser entering the interferometer to be adjusted. The portion of the beam transmitted through PBS 1 is p-polarized and is sent to the interferometer, while the

s-polarized reflection from PBS 1 is absorbed by a damper. By adjusting the polarization angle of the HWP the fraction of the beam transmitted can be easily adjusted. Since the board that captures the PDs signals has a dynamic range of ±10V, the power of the laser should be adjusted so that the full dynamic range is used without saturating the PDs.

Pumping System

A three stage pumping system is used to both lower the pressure to the desired pressure and maintain the pressure duing data collection. Two of the stages of the pumping are performed in order to lower the pressure to the operational pressure of the final pump, which is used to maintain the vacuum.

The first stage of pumping is a scroll pump that is external to the lab/clean room. The pump is attached through a piping system that leads outside the lab. The scroll pump only needs to be run on the order of tens of minutes, starting from atmospheric pressure, before the next stage of the pump can be engaged at a chamber pressure of around 10^{-1}-10^{-2}mbar. The next stage of pumping is performed using a turbopump that is mounted to the vacuum system on the experimental setup and has a maximum pumping rate of around 77 liters/s for dry air. This stage of pumping can bring the system pressure down to $\sim 10^{-5}$ mbar. The turbopump is run in series to the scroll pump, however unlike the scroll pump alone, the turbopump needs to run on the order of tens of hours to days to achieve the desired pressure to engage the final pumping stage. This significant time investment in re-establishing the vacuum in the chamber means that the chamber is only pressurized when it is strictly necessary.

The final stage of pumping is done by an ion pump mounted to the optical bench. This pump can only be started when the chamber pressure is already on the order of $\sim 10^{-4}$mbar, and ideally closer to $\sim 10^{-5}$mbar. The ion pump is not capable of pumping air above this pressure, and typically does not obtain significantly lower pressure than the pressure it is started at, if lower at all. However, unlike the scroll and turbopump, the ion pump runs without any vibration, and so is ideal for a use case such as this where minimization of noise is paramount.

3 Interferometric Readout and Lorentzian Fitting

This chapter discusses how the data captured by the photodiodes (PDs) are analyzed to extract the motion of the oscillator; it describes the ideal optical response, the real PD output, and how the data are combined to adjust for imperfections in the optics and PDs. This is followed up by a discussion of how the effective temperature is estimated from the power spectral density (PSD) around the resonance of the first longitudinal mode of the oscillator.

3.1 Idealized Interferometric Readout

We are now interested in finding the intensity of the light at each photodiode in the ideal case. To find this we adopt Jones formalism, where the electric field is represented by a vector of length two, and each optical component by a 2x2 matrix [23]. We can express the polarization of the beam using its x and y axis components. The Jones matrices of relevant components are shown in table 3.1.

Component	Symbol	Jones Matrix
Mirror	J_M	$\begin{pmatrix} 1 & 0 \\ 0 & -1 \end{pmatrix}$
Beam Splitter	J_{BS}	$\frac{1}{\sqrt{2}}\begin{pmatrix} 1 & 0 \\ 0 & 1 \end{pmatrix}$
$PBS_{transmitted}$	J_{PBSt}	$\begin{pmatrix} 1 & 0 \\ 0 & 0 \end{pmatrix}$
$PBS_{reflected}$	J_{PBSr}	$\begin{pmatrix} 0 & 0 \\ 0 & 1 \end{pmatrix}$
HWP at 22.5°	J_{+HWP}	$\frac{1}{\sqrt{2}}\begin{pmatrix} 1 & 1 \\ 1 & -1 \end{pmatrix}$
HWP at -22.5°	J_{-HWP}	$\frac{1}{\sqrt{2}}\begin{pmatrix} 1 & -1 \\ -1 & -1 \end{pmatrix}$
QWP at 45°	J_{QWP}	$\frac{1}{\sqrt{2}}\begin{pmatrix} 1 & i \\ i & 1 \end{pmatrix}$

Table 3.1: Table of all of optical components used in the experimental setup and their Jones matrices.

We track the electric field of the beam starting with the beam entering PBS #1 (as can be seen in figure 2.6), $\vec{E}_{\text{in}}$, after traveling through the HWP after the telescope. After exiting the PBS the beam can be described as:

$$\vec{E_0} = J_{PBSt}\vec{E}_{in} = E_{in}\begin{pmatrix} 1 \\ 0 \end{pmatrix} \tag{3.1}$$

The beam then passes through a 50:50 BS (BS#1) and HWP#2 before arriving at the chamber. The BS sends half of the beam towards the chamber and the other half towards a damper. A beam splitter is used over a mirror in order to separate the returning beam and redirect it towards the readout PDs. HWP#2 then has its fast axis set to 22.5°in order to rotate the beam by $\pi/4$ and split the power equally between the x and y polarizations. The beam that enters the chamber is described by:

$$\vec{E}_{chamber} = J_{+HWP}J_{BS}\vec{E_0} = \frac{E_{in}}{2}\begin{pmatrix} 1 \\ 1 \end{pmatrix} \tag{3.2}$$

Inside the chamber the beam encounters PBS#2. The p-polarization is transmitted to the mirror on the oscillator, and the s-polarization is reflected to the reference mirror. After reflection and upon returning to PBS#2 these two beams can be described as:

$$\vec{E}_{oscillator} = J_M J_{PBSt} \vec{E_{chamber}} = \frac{E_{in}}{2} e^{i2k(L_O+\delta_x)} \begin{pmatrix} 1 \\ 0 \end{pmatrix} \tag{3.3}$$

$$\vec{E}_{reference} = J_M J_{PBSr} \vec{E}_{chamber} = \frac{E_{in}}{2} e^{i2kL_R} \begin{pmatrix} 0 \\ -1 \end{pmatrix} \tag{3.4}$$

L_O and L_R represent the path distance of the light going from PBS#2 to the respective mirror and back, with δ_x representing the displacement of the oscillator, and where $k = \frac{2\pi}{\lambda}$. The two beams are recombined at the oscillator so that the beam exiting the chamber can be described as:

$$\vec{E}_{exit} = \vec{E}_{oscillator} + \vec{E}_{reference} = \frac{E_{in}}{2} \begin{pmatrix} 1 \\ -e^{i\psi} \end{pmatrix} \tag{3.5}$$

Here we write $\Delta\psi = 2k(L_R - L_0 - \delta_x) = 2k(\Delta L - \delta_x)$ and we take out a phase factor common to both polarizations.

The beam then travels back through HWP#2 so that it sees the fast axis at -22.5°, and returns to BS#1. The transmitted half of the beam is absorbed by a damper near PBS#1 this time through (not shown in figure 2.6), with the reflected portion of the beam that passes through the iris and steering mirrors (which were added during this work and were instead shown in figure 4.6), arriving at the detection area, described as:

$$\vec{E}_{detection} = J_{BS} J_{-HWP} \vec{E}_{exit} = \frac{E_{in}}{4} \begin{pmatrix} 1 + e^{i\psi} \\ -1 + e^{i\psi} \end{pmatrix} \tag{3.6}$$

Once inside the detection area the beam passes through BS#2, sending the transmitted portion to PDs C and D, and the reflected portion to PDs A and B. The portion of the beam reaching PBS#3 is described as:

$$\vec{E}_{AB} = J_{BS} \vec{E}_{detection} = \frac{E_{in}}{\sqrt{32}} \begin{pmatrix} 1 + e^{i\psi} \\ -1 + e^{i\psi} \end{pmatrix} \tag{3.7}$$

The beam in the AB arm is then split by PBS#3 to send the p-polarized portion to photodiode A, and the s-polarized portion to photodiode B. The two beams arriving the the two PDs can be described as:

$$\vec{E}_A = J_{PBSt} \vec{E}_{AB} = \frac{E_{in}}{4\sqrt{2}} \begin{pmatrix} 1 + e^{i\psi} \\ 0 \end{pmatrix} \tag{3.8}$$

$$\vec{E}_B = J_{PBSr} \vec{E}_{detection} = \frac{E_{in}}{\sqrt{32}} \begin{pmatrix} 0 \\ -1 + e^{i\psi} \end{pmatrix} \tag{3.9}$$

The part of the beam sent to the CD arm then passes through QWP#1 before reaching PBS#4 and splitting to send the p-polarized beam to photodiode D and the s-polarized beam to photodiode C. QWP#1 shifts the relative phase of the two polarizations by $\frac{\pi}{2}$ so that by using all four PDs the full optical phase of the beam can be extracted. The beam that arrives at PBS#4 is described as:

$$\vec{E}_{CD} = J_{QWP} J_{BS} \vec{E}_{detection} = \frac{E_{in}}{8} \begin{pmatrix} 1 + e^{i\psi} - i + ie^{i\psi} \\ -1 + e^{i\psi} + i + ie^{i\psi} \end{pmatrix} \tag{3.10}$$

With the two beams then reaching PDs C and D described as:

$$\vec{E}_C = J_{PBSr}\vec{E}_{CD} = \frac{E_{in}}{8}\begin{pmatrix} 0 \\ -1 + e^{i\psi} + i + ie^{i\psi} \end{pmatrix} \tag{3.11}$$

$$\vec{E}_D = J_{PBSt}\vec{E}_{CD} = \frac{E_{in}}{8}\begin{pmatrix} 1 + e^{i\psi} - i + ie^{i\psi} \\ 0 \end{pmatrix} \tag{3.12}$$

For each of the four PDs the incident power is:

$$P_A = \frac{P_{in}}{16}(1 + cos(\psi)) \tag{3.13}$$

$$P_B = \frac{P_{in}}{16}(1 - cos(\psi)) \tag{3.14}$$

$$P_C = \frac{P_{in}}{16}(1 + sin(\psi)) \tag{3.15}$$

$$P_D = \frac{P_{in}}{16}(1 - sin(\psi)) \tag{3.16}$$

Using each pair of PDs (A and B, C and D) we can unambiguously extract the phase. Equations 3.13 and 3.14, and 3.15 and 3.16 can be combined to get equations 3.17 and 3.18, respectively:

$$cos(\psi) = \frac{P_A - P_B}{P_A + P_B} \equiv C_x \tag{3.17}$$

$$sin(\psi) = \frac{P_C - P_D}{P_C + P_D} \equiv C_y \tag{3.18}$$

C_x and C_y are here referred to as the "contrasts" of the two pairs of PDs. We can then use $cos(\psi)$ and $sin(\psi)$ to unambiguously retrieve the phase using the four quadrant arctangent function. Using the power relations obtained in equations 3.13 through 3.16 we can also simplify equations 3.17 and 3.18 to show that the contrasts are power independent.

We also define the complex contrast as C:

$$C \equiv C_x + iC_y = e^{i\psi} \tag{3.19}$$

Using quadrature phase differential interferometry (QPDI) to find C_x and C_y allows us to directly find ψ here when displaying C in the complex plane. This means we can display C as a unit circle centered on (0,0). Knowing this, we can use any one measurement from the PDs to find the phase angle.

We previously defined ψ as part of equation 3.5 as:

$$\Delta\psi = 2k(L_R - L_O - \delta_x) = \frac{4\pi}{\lambda}(\Delta L - \delta_x) \tag{3.20}$$

We can also derive equation 3.19 to get:

$$\frac{dC}{d(\delta x)} = \frac{4\pi}{\lambda} \tag{3.21}$$

In equation 3.20, ΔL represents the optical path difference between the two arms of the interferometer, which may vary slowly over time due to thermal drift or mechanical effects. δ_x is from the displacement of the oscillator. Since these two quantities are summed, and we are working with phase (which is of course cyclical with a period of 2π), ΔL does not impact

the sensitivity of the system and can be treated only as a point that δ_x oscillates around, as long as ΔL slowly compared to δ_x and so can be separated in frequency.

Once we are able to find the optical phase, we can find the displacement directly from:

$$\Delta L - \delta_x = \frac{\lambda}{4\pi}\Delta\psi \tag{3.22}$$

In the frequency regime around the resonant frequency of the oscillator, the rate of change of ΔL is negligible, as the drift in interferometer arm length happens at much lower frequencies. At this regime we can treat ΔL as static and so for frequencies at or above the resonant modes of the oscillator we can treat equation 3.22 to be:

$$\delta_x = \frac{\lambda}{4\pi}\Delta\psi \tag{3.23}$$

This is useful for the experiment as, while ΔL may drift over time, it does not need to be corrected for since its drift does not impact the frequency range we are interested in.

3.2 Calibration and Real Measurement

The previous section discusses the ideal perfect case of the expected power and contrasts that we would expect to see. Various imperfections and misalignments with the various optical elements cause variation from the ideal case. For example, mirrors and beam splitters do not consistently reflect different polarizations the same as each other, resulting in different behavior for the different polarized portions of the beam. Similarly, the beam splitters do not perfectly reflect and transmit the light exactly 50:50.

Equations 3.17 and 3.18 led us to represent the phase as a perfect circle when finding the contrast as a function of the phase. In the real case, the plot of the contrast will be non-circular, closer to an ellipse.

In the real system, a calibration needs to be performed in order to correct for the deviation of the contrast from the ideal. The contrast is acquired over a range for ψ of at least 2π to give the full contrast curve. The curve is then fit by performing a Heydemann correction, giving an ellipse that attempts to fit the real [24].

Initially, the method used to explore the full phase was to use the piezoelectric actuator the reference mirror was mounted to to displace the reference mirror and change the path length L_R. The piezoelectric actuator would have a sinusoidal voltage applied in order to create this displacement.

After this actuator was removed from the experimental setup, as discussed in section 4.1, this method was no longer possible. The new method of acquiring a calibration curve was by using the IR heater to cause the oscillator to expand, this time changing L_O instead of L_R. This thermal expansion is sufficient to acquire multiple full phases in a reasonable period of time. The previous method using the actuator would be used to acquire data for the calibration over a time period on the order of 5-10 seconds. Although longer, the thermal expansion method can still acquire sufficient data for a calibration over a time period on the order of 1-3 minutes.

The power across the PDs is then used to find C_x and C_y as the working point, which is the location on the contrast circle/ellipse that represents the phase of the interferometric output by way of the displacement of the oscillator, is varied. This curve could be fitted to find the parameters X_0, Y_0, X, Y, and ϕ:

$$C_x = X_0 + Xcos(\psi) \tag{3.24}$$

$$C_y = Y_0 + Y sin(\psi + \phi) \tag{3.25}$$

X_0 and Y_0 represent the center of the resulting fitted ellipse, X and Y are the projection of the semimajor axes on the x and y axes, and ϕ is the precession. Using these parameters, we can solve for ψ, which can also be used to find the displacement δ_x.

$$cos(\psi) = \frac{C_x - X_0}{X} \tag{3.26}$$

$$sin(\psi) = \frac{C_y - Y_0}{Y cos(\phi)} - \frac{C_x - X_0}{X} tan(\phi) \tag{3.27}$$

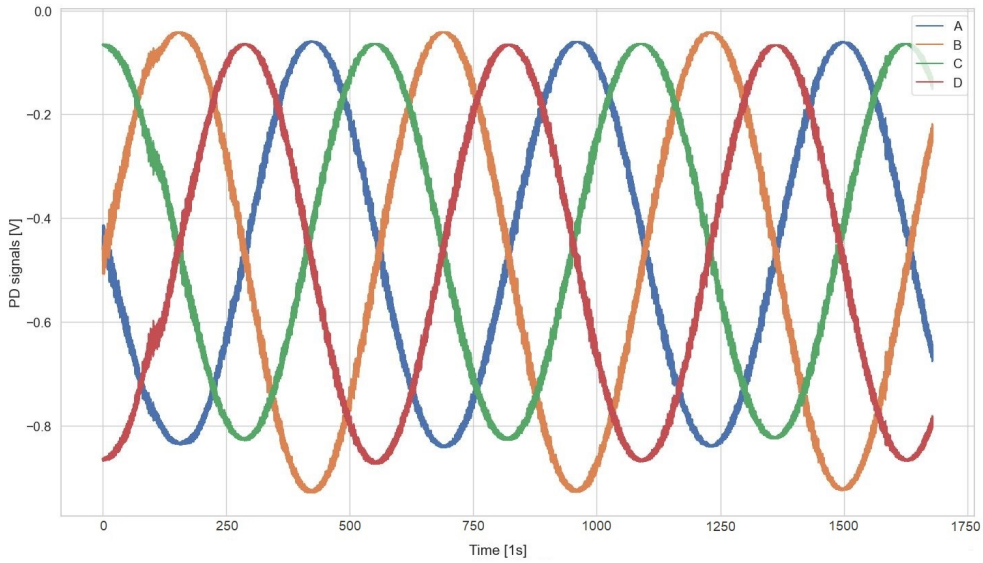

(a) PD output during calibration.

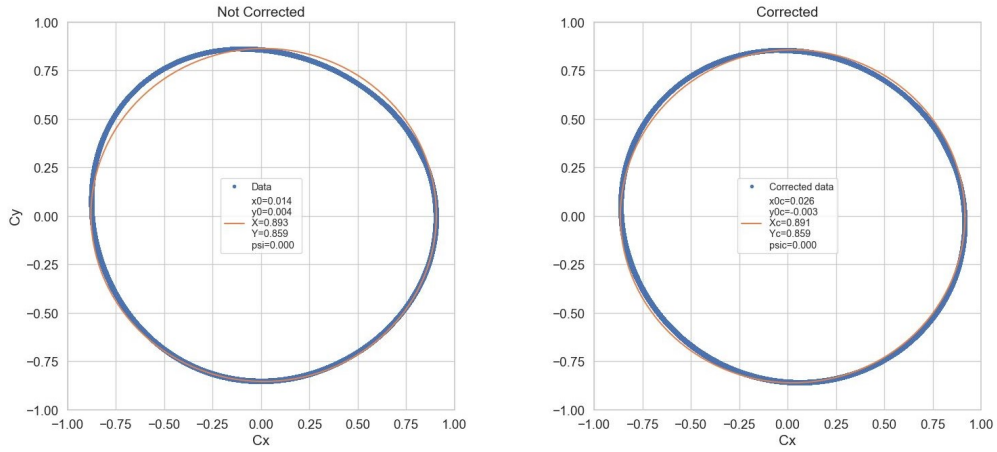

(b) Contrast curve before and after fitting.

Figure 3.1: Example of the calibration done using the IR heater. (a) Measured output of the PDs while the IR heater is causing the oscillator to thermally expand. The total time of acquisition here is just under 3 minutes. (b) Contrast of the same set up date before and after correcting, as discussed in section 3.2. The ellipse fits are displayed in orange, and the corrected/uncorrected data is displayed in blue. The parameters X_0, Y_0, X, Y, and ϕ of the ellipses are also displayed.

One other calibration process was also performed for when the data collection was done while the temperature of the chamber was varied. During the heating process, the thermal expansion of the chamber can be expected to be of larger magnitude than what is typical in the climate controlled lab at room temperature, and this expansion is likely not homogeneous. Due to the combination of these factors and the fact that the heating process takes many hours to days, it is useful to be able to create calibrations from the fast data recorded for experimental purposes without having to perform the previously discussed calibration method.

Since the chamber is changing temperature, the length of the oscillator changes (similarly to how it would when using the IR heater), so the fast data collected for the experiment can be used to create a calibration file. The temperature change in this way is significantly more gradual than when using the IR heater for calibration, as the chamber changes temperature more slowly. The fast data can be decimated in order to reduce the amount of data down to a manageable amount for the creation of a calibration file while still containing the behavior of the phase. An example of this type of calibration can be seen in figure 3.2.

It can be noted that the contrast ellipses do not "close" for these calibration methods. The contrast ellipses collected as part of the previously discussed method appear as closed ellipses where the start and end of the calibration curve overlap; this is not the case for the ellipses made from the experimental data. This is due to the fact that, as previously discussed, the contrast ellipse changes as the chamber heats up, and the contrast ellipse can cover a period of many hours in which the chamber heats up sufficiently to change the shape of the ellipse as the alignment of the system changes due to thermal expansion. Since the changes in the calibration curve are small in magnitude, this "average" calibration curve of this longer period of data collection is sufficient to correct the data for the period it represents. These calibrations were also checked for each set of data for which they were used to ensure that there were no poor fits.

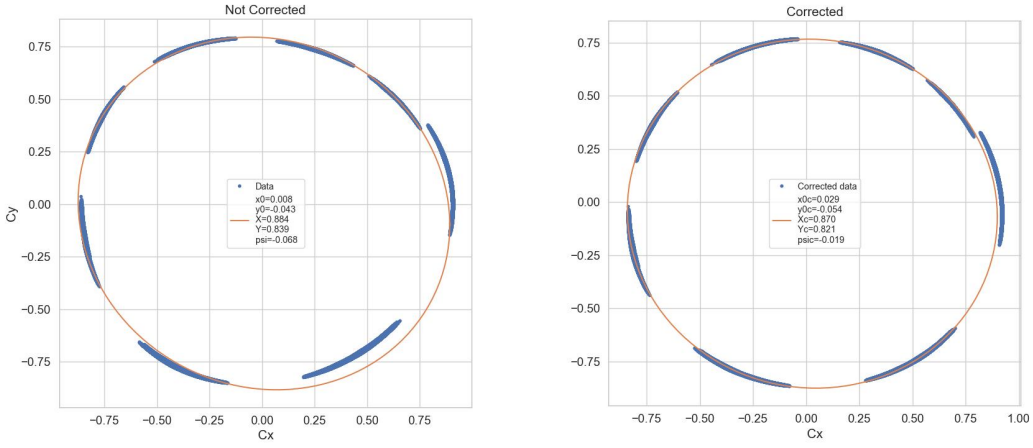

Figure 3.2: Calibrated contrast circle made from decimated PD data. Fast data collection was typically done with a cadence of one hour of data collection with a two hour pause before the next set. These gaps in data collection can be seen in the data here where the temperature of the experiment increased and the phase progressed while no data was being collected. The left figure shows the calibration circle before correction, and the right figure shows the calibration circle after correction.

3.3 Spectral Analysis

The end point of this analysis is to find the effective temperature (T_{eff}) of the oscillator. In order to do this, we must be able to investigate the behavior of the oscillator at its resonant

frequencies. This section explains how the power spectral density (PSD) is found, what contributes to it, and how selection of good stretches of data are made using white noise as an indicator.

Power Spectral Density of Displacement

The ability of the experiment to detect the displacement of the oscillator, δ_x, is limited by the sources of noise at a given frequency. Several noise sources contribute to the signal measured in the NETN experiment, many of which directly affect δ_x, which are a part of the ideal component of the signal $S_{\delta x}^{ideal}$, representing the signal caused by displacement and mechanical noise. Other noise sources that affect detection are, primarily: shot noise of the PDs and limitations of the resolution of the PD acquisition board, represented by $S_N(v)$. This gives us the following equation representing the total PSD:

$$S_{\delta x}(v) = S_{\delta x}^{ideal}(v) + S_N(v) \tag{3.28}$$

Signal acquisition during fast data collection is performed by collecting 20 minute files at a sampling frequency of 8kHz. As discussed in section 3.2, the signal is corrected using the calibration file containing the parameters discussed in section 3.2. The phase obtained from this process is then used to find the effective displacement due to oscillations and drift in the path length difference of the interferometer arms as shown in equation 3.22, which as discussed when introducing equation 3.23 can be considered to be the oscillator displacement only at high frequencies. From here we wish to produce a PSD of this effective displacement so that the high frequency effects can be separated from the low frequency drift of the arm lengths. The series of δ_x is broken into sections of $T = 20$ seconds each and a PSD for each is produced using the Fast Fourier Transform. The resulting transform has a frequency resolution of $\delta_f = 1/T = 0.05Hz$.

White Noise

The NETN experiment is somewhat sensitive to environmental disturbances and other variations in the apparatus performances, and because of this, some data will need to be rejected. A method of rejecting data due to high levels of environmental noise or poor fitting is needed to ensure the quality of the data that is used.

A typical PSD of the signal measured by the PDs can be seen in figure 3.3, with the longitudinal resonance peak shown more closely due to its importance to the experiment. A region just below the frequency of the longitudinal resonance peak of the oscillator can be selected to investigate the white noise, the constant intensity continuum noise, near the peak. This region can be found from inspection of a PSD that is generated from the first 6 minutes of data after a new acquisition is started by choosing a region free of peaks that is close to, but not overlapping, the resonant peak. Since the frequency of the resonant peak does not change by more than a few Hz between different sets of data collection, so the same region (1365-1390 Hz) can generally be used between different data collection runs. The average white noise can be found for each of the 20-second sections of data. The average white noise of each section of the data is then arranged in a histogram, as can been seen in figure 3.4. A threshold level is chosen as a compromise between cutting off too many data while still cutting off the upper tail of spectra with high white noise continua; any 20 second data segment in this region with an average noise above this threshold is discarded.

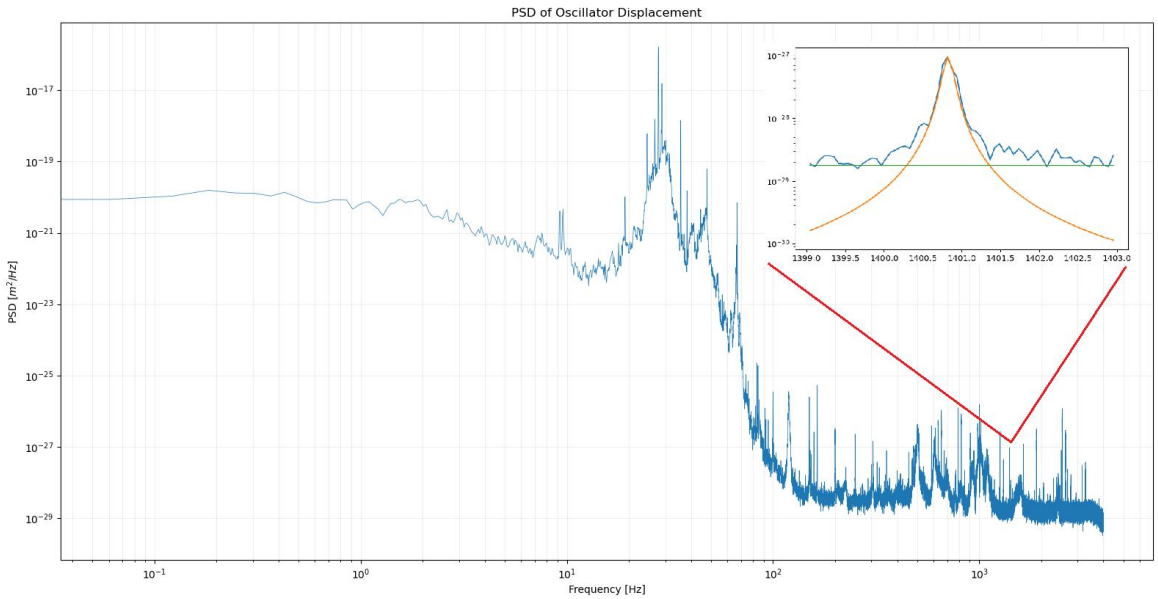

Figure 3.3: The main body of the figure shows a typical PSD figure for the NETN experiment, with this specific PSD representing a 20 second section of fast data from May 2 2024. Typically, the continuum of the background noise at high frequency is around 10^{-28}-$10^{-29}\frac{m^2}{Hz}$. For finding T_{eff} the noise continuum should be low enough such that the longitudinal resonant peak has larger magnitude in the region around its peak than the magnitude of the continuum. The sub-figure shows the PSD around the longitudinal resonant frequency of the oscillator, with the orange curve representing the Lorentzian peak fit, and the green horizontal line representing the average white noise level in the region just below the peak.

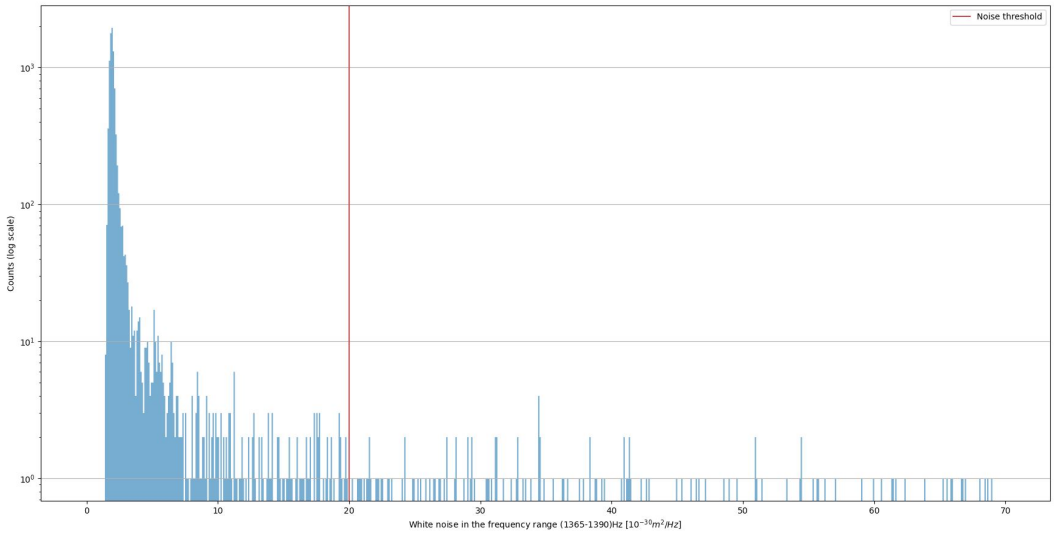

Figure 3.4: Example of a histogram of the white noise average levels of the 20 second PSDs discussed in section 3.3. These white noise levels correspond to to data taken from April 30 2024 to May 3 2024. The red line represents a noise level of $2x10^{-29}m^2/Hz$, a threshold chosen to cut off the tail of the histogram. Any PSDs that exceed this threshold are discarded.

3.4 Effective Temperature Calculation

Estimating a PSD of a time series carries a new problem with it, which is that each point has a very large uncertainty, with the uncertainty of each point in a single PSD being equal to the value of the point itself. To reduce the uncertainty, if we assume that all the spectra we find are the result of the same underlying stationary process, we can average N spectra to reduce the uncertainty on each point by a factor of $\sqrt{N}$. We have chosen to average 20 spectra, resulting in a reduction in uncertainty by a factor of more than 4.

We then fit the resonant peak of the longitudinal mode of the oscillator on each of these average spectra. This peak is typically around 1400Hz, and tends to be above 1400Hz at room temperature (approximately 297K), and will be just below 1400Hz at higher temperatures. The fitting is performed in a region approximately ±3Hz around the resonant peak. There are two parts to the fit; the first being similar to what was performed in the previous section where the white noise is fit by looking at the region just below the resonant peak in order to have a range of frequencies free of peaks, but still close to the peak of interest. The second component of the fit is a Lorentzian fit of the resonant peak. Both of these components of the fit can be added together to give:

$$y(\nu) = y_0 + \frac{2}{\pi} A \frac{\Delta\nu}{4(\nu - \nu_0)^2 + \Delta\nu^2} \tag{3.29}$$

Here, y_0 represents the white noise continuum. The second term represents the Lorentzian fit with A representing the area of the peak, $\Delta\nu$ is the full width at half maximum, and ν_0 is the resonant frequency or the frequency at the peak.

After finding each of these parameters for each fit we also find a reduced χ^2_R for each spectra, where a fit is rejected if its χ^2_R value is higher than a threshold $\chi^2_{R\,threshold}$, defined as $P(\chi^2_R > \chi^2_{R\,threshold}) = 5\%$. Figure 3.5a shows an example of the parameters found from the spectra fits, with the passing fits shown in red.

Once the area and resonant frequency of the longitudinal mode have been obtained T_{eff} can be found using the following formula (the discussion of the theory of effective temperature calculation can be found in section 1.4):

$$T_{eff} = \frac{m \cdot (2\pi\nu_0)^2 \langle x^2(t) \rangle}{k_B} \tag{3.30}$$

Here, m = 0.333 kg is the mass of the oscillator and $\langle x^2(t) \rangle$ = A is the mean square longitudinal displacement caused by thermal noise. Conditions are treated as stationary over any given selected stretch of data, so the values of T_{eff} are fit to a Gaussian curve, where the mean value after selection of χ^2_R yields $\mu = T_{avg}$, which is the estimation of the effective temperature for the measurement period.

(a) Parameters of the Lorentzian fit.

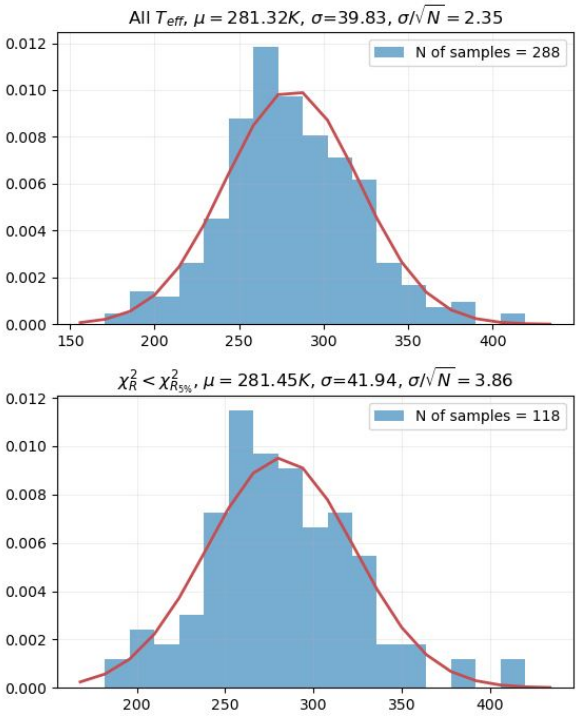

(b) Histogram of T_{eff}

Figure 3.5: Both figures are from the analysis done on data collected from April 30 2024 through May 1 2024. (a) Parameters found from performed Lorentzian fits on the longitudinal resonant peaks of the averaged spectra. The x-axis is an index number. The points in red are the ones that passed a reduced χ^2 selection. (b) Shows two histograms representing T_{eff} before (above) and after (below) the same reduced χ^2 selection. Also reported are the mean T_{eff} of each histogram, shown as μ, and the normal and reduced standard deviations (σ and $\sigma/\sqrt{N}$), respectively.

4 Upgrading the Experimental Setup

The beginning of this thesis work did not coincide with the beginning of the NETN experiment, which was started initially in 2019. The goal of this experiment has been to be able to obtain sufficient stability in measurements of effective temperature, and so, thermal noise, so that changes in it can be observed from experiments to better understand NETN. While this thesis project worked towards the goal of being able to consistently measure effective temperature, and to detect changes in T_{eff} as the thermodynamic temperature is changed, a significant amount of time had to be dedicated to making changes and upgrades to the experimental setup.

4.1 Reference Mirror Problems

At the start of this thesis work the very first trials with the chamber temperature elevated above room temperature were being performed. One of the main purposes of this data collection was to confirm that the experimental setup could still collect data of the same quality as it had at room temperature. One of the simplest tests of this was to see if the sum of the voltage measured across all four photodiodes stayed roughly constant over time. A hard limit for "roughly constant" was not established but variance of greater than a few percent would not be expected over any time scale if the experimental setup were not disturbed.

As can be observed in figure 4.1, the data from this period show a significant variance in the amount of voltage measured by the PDs, which is representative of the amount of incident laser power. The four PDs are each capture part of phase of the light returning from the interferometric arms (as discussed in chapter 2), and so when the power from all four is added up it should remain constant over time with minor fluctuations as the four PDs should be capturing all of the polarizations of beam. It can be observed that this was not the case during the period of time shows in figure 4.1. Not only was the measured power not constant, but it was varying wildly (with the behavior in the center part of the figure being more typical of what would be measured) over time without anything physically being changed in the experiment.

This began a period of significant investigation to be able to understand the issue of inconsistent voltage shown in figure 4.1. In order to be able to understand this unexpected behavior we first checked the optical alignment of the system and found a spurious beam returning from the vacuum chamber.

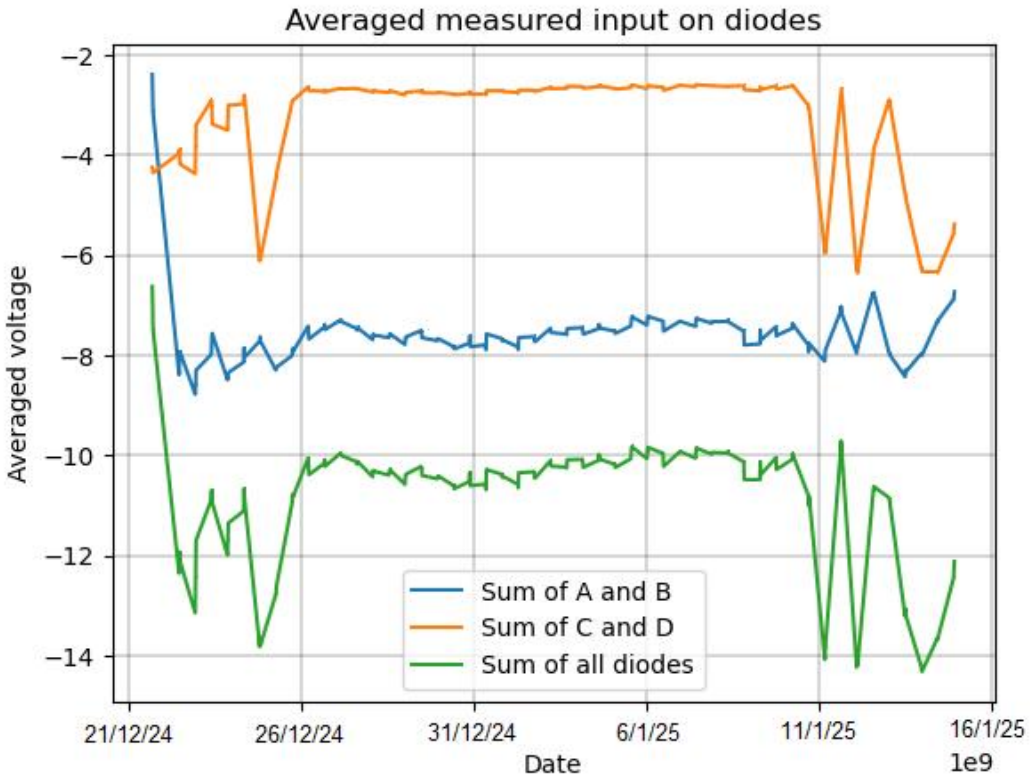

Figure 4.1: Voltage measured across the two pairs of photodiodes vs time, and total voltage measured across all four. During this period of data collection the temperature of the chamber was elevated by ∼25K above room temperature to ∼318K. The total voltage across all four PDs should be roughly constant over time but was not here.

To investigate this, we took advantage of the fact that the beams returning from the chamber reflected by the reference mirror or oscillating mass would have orthogonal polarizations due to the fact they were split using the PBS inside of the chamber. Using the half-waveplate (HWP#1, as can be seen in figure 4.6) the polarization of the beam entering the chamber can be adjusted in order to isolate one of the two returning beams based on the angle to which it is set, so that nearly all of the laser light would be directly to one of the two mirrors. Here we wanted to use HWP#1 to test if the two returning beams did, in fact, have opposite polarizations. If one beam was returning from the oscillator and the other from the reference mirror, it would be expected that changing the angle of HWP#1 would allow each beam to be isolated when the polarization of the beam entering the chamber would be entirely either transmitted or reflected by the PBS.

HWP Angle (degrees)	Total Power	Power at PDs	Secondary Reflection Power
289	15.7mW	3.2mW	5.4mW
266	10.7mW	0.033mW	10.7mW
312	6.7mW	6.7mW	0mW
0 (removed HWP)	15.7mW	0mW	11.3mW

Table 4.1: Effect of changing the angle of HWP#1 on the power measured by the PDs and the secondary reflection noticed during the initial troubleshooting after heating. The angle is the angle that HWP#1 is set at. Total Power represents the power measured exiting the HWP at the corresponding angle. The third column is the power measured entering the detection area with the photodiodes, and the fourth column is the power of the spurious reflection measured after it exits the chamber and before HWP#1.

As can be seen in table 4.1 the two beams appeared to have opposite polarizations. By adjusting the angle of the HWP the power of one beam could be reduced to ∼0mW, and by rotating the HWP by ∼45 degrees the opposite beam could be reduced to ∼0mW. This heavily suggested that the problem that the experiment was facing was that the two beams from the two interferometric arms had become misaligned, presumably from having heated the experiment for the first time.

The fact that increasing the temperature of the experiment by ∼25K had resulted in a significant misalignment of the experiment was extremely problematic. The design of the experiment was not compatible with the alignment of the experimental setup being so heavily dependent on the temperature.

Since the tests summarized in table 4.1 indicated that one of the arms was misaligned, and that alignment could not be recovered using the external optics, we decided to open the vacuum chamber.

The reflective surface on the oscillator mass cannot be easily adjusted, but the reference mirror can be (once the chamber is opened), allowing the two beams to be aligned again. As discussed in section 2.1, the reference mirror was glued to a piezoelectric actuator so that a change in the relative position of more than a fringe could be introduced into the interferometer, and the assembly of the actuator and the reference mirror were mounted in a kinematic mount. The process of aligning the system involved first a coarse alignment by overlapping the two beams using a standard infrared card, and then maximizing the voltage measured by the PDs to maximize the contrast by making fine adjustments to the reference mirror. This seemed to solve the problem, the contrast was brought back to typical levels, and the chamber was closed.

Unfortunately, the did not solve the problem and behavior similar to what was observed in figure 4.1 was observed again. As a result, the chamber had to be reopened.

It was observed that if the system was properly aligned so that the contrast was optimized, any sudden change in the distribution of the mass of the chamber would immediately throw off the alignment of the optics. During the reassembly of the chamber even a very mild impact of replacing chamber components would ruin the alignment.

During our investigation of these unexpected behavior we also compared the PSD of the interferometer during this period as compared to a period of typical operation of the experiment before the first trials where the experiment was heated with the heating coil (which seems to have created this unexpected behavior). The background noise continuum of the PSD of figure 4.2 (as can be seen in the bottom part of the figure) shows that the magnitude of the background noise was over an order of magnitude higher during this period than during the previous period before when the chamber had been heated for the first time.

The primary problem this caused is that the longitudinal resonant peak would be "lost" due to the continuum being of larger magnitude than the resonant peak, as discussed in section 3.3. This change in the noise continuum of the PSD was very unexpected and indicated a problem with the experiment outside of pure alignment issues.

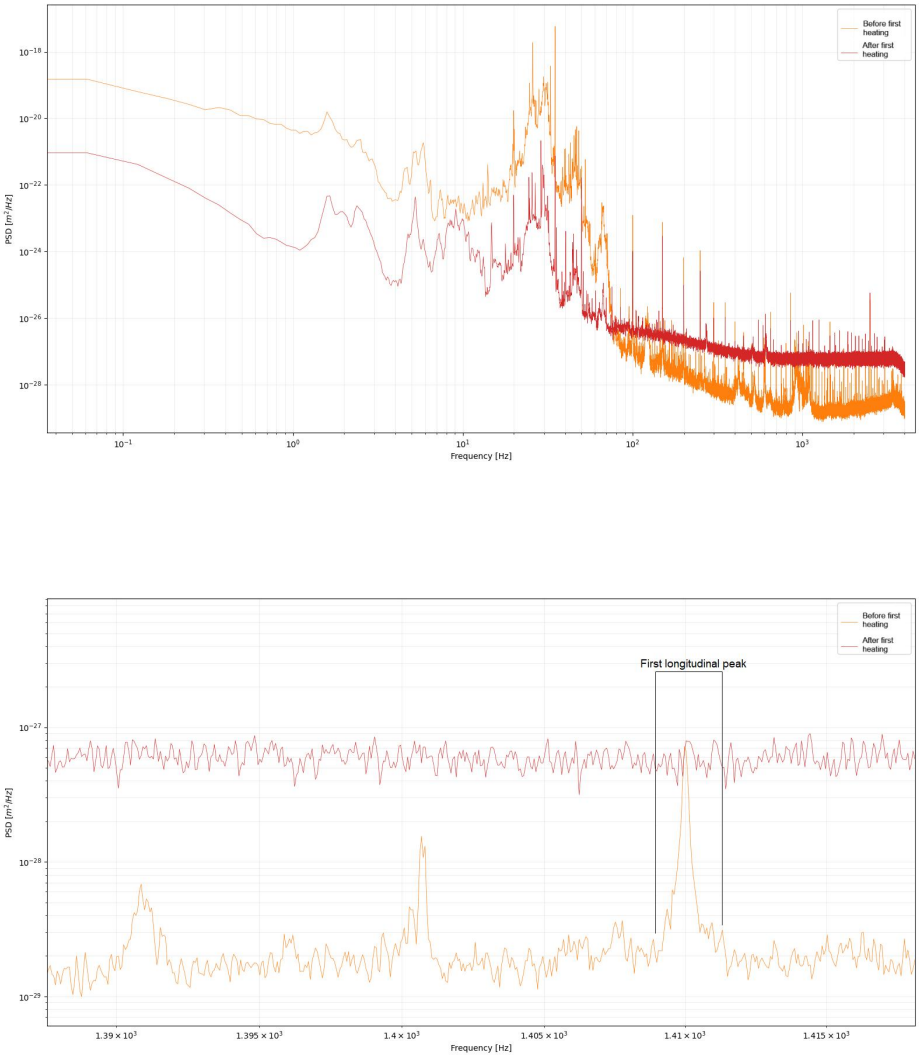

Figure 4.2: Comparison of the PSDs between the period when the experiment was working as expected before it had been heated with the heating coil for the first time (orange, lighter) and when the reference mirror was poorly attached (red, darker). The bottom image is zoomed in around the frequency where the longitudinal resonant frequency mode is.

At this point, the chamber was opened and the bracket was removed. Immediately, the source of the problem was found, the reference mirror was no longer in place glued to the piezoelectric actuator, but instead was found lying on the floor of the vacuum chamber (as can be seen in figure 4.3). It is likely that the mirror had become loosely attached during the heating phase, which is why the alignment of the chamber would change so drastically over short periods of time as the mirror moved around. While it isn't possible to precisely know when the mirror came fully detached, it seems likely it was during one of the recent attempts

to align the system.

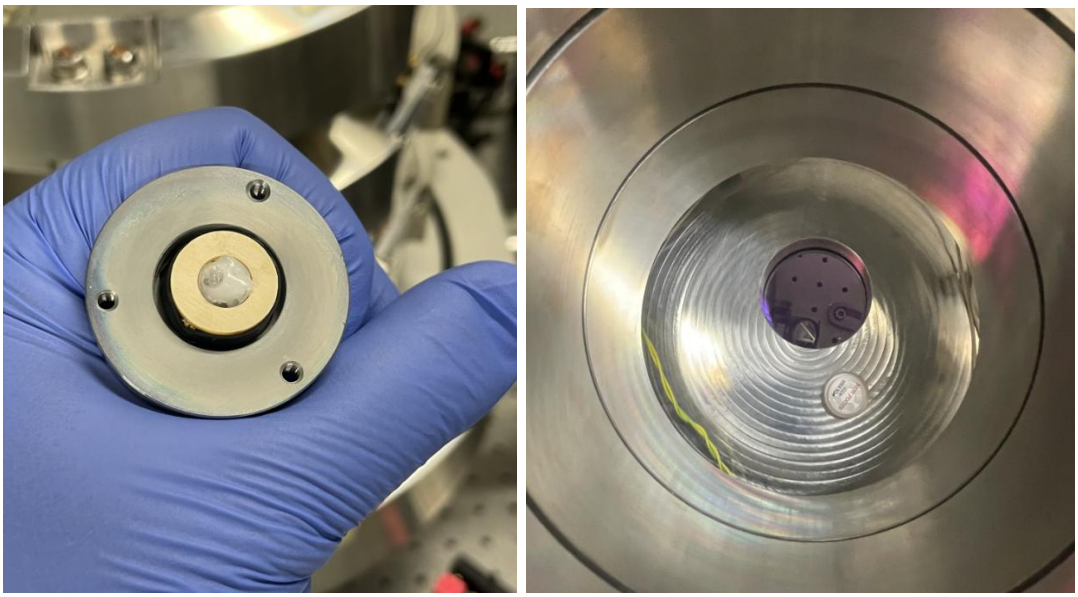

Figure 4.3: These two images show the glue that had melted allowing the reference mirror to detach from the piezoelectric actuator, and the detached mirror that was discovered at the bottom of the vacuum chamber.

The next step was clearly to replace the mirror. A new mirror that met the same specifications as the previous one was chosen, however we wanted to avoid using glue to avoid replicating the problem that caused the mirror to detach. Instead we decided to remove the piezoelectric actuator, due to suspecting that it introduced fluctuations in the displacement of the mirror which would affect measurement of the effective temperature, and attached the mirror directly by securing it with the adjustable mount the actuator-mirror assembly had been secured by previously. The piezoelectric oscillator was useful for investigating the contrast and acquiring calibration files, but both of these purposes could be satisfied by manually tapping the chamber (for quick viewing of the contrast for alignment) and using the IR heater (for calibration and checking to make sure the contrast is acceptable).

After this new mirror was put in place, the chamber could be aligned and retain that correct alignment over time. It is also worth noting that in order to remove the piezoelectric oscillator the PBS attached to the bracket (as can be seen in 2.1a) also had to be removed and put back in place after this change was made.

4.2 Upgrades and Realignment

Before discussing the upgrades/changes made to the experiment, one of the problems that led to some of these changes needs to be discussed. After reassembling the chamber after replacing the reference mirror, as noted in the previous section, a new problem was found with the experimental setup. The way the experiment had been run was to have both beams coming from the two interferometric arms be coincident with each other. As stated in section 4.1, these beams had previously been found to be out of alignment with each other, and the way that the two beams were differentiated from each other was by adjusting the HWP they passed through because they were perpendicularly polarized relative to each other.

Once the reference mirror was aligned again and the chamber was closed, a new alignment

issue was found. Instead of one single spot representing the beam returning from the interferometer arms, there was now a single brighter spot with two lower intensity spots on either side of it, as can be seen in figure 4.4.

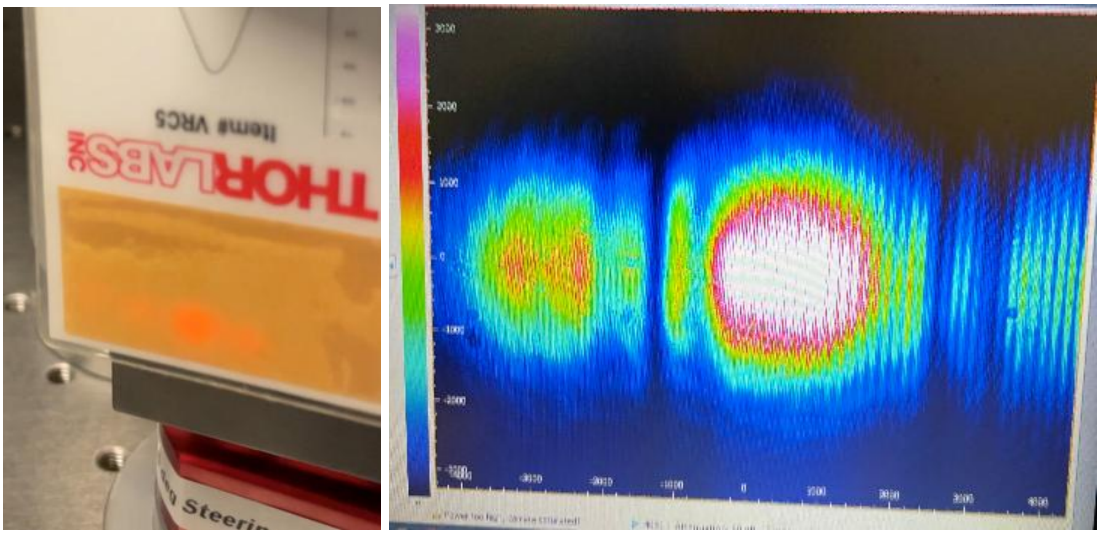

Figure 4.4: The three reflections observed after replacing the reference mirror as observed with a laser viewing card (left) and the beam profiler (right).

As can be seen in figure 4.4, the spots are difficult to observe any detail with by eye. This observation was performed with laser viewing cards, which allow the infrared beam to be seen, but were not convenient for longer observations or good at showing necessary detail.The best way to investigate this was with a beam profiler, but the way the experiment was structured made it difficult to interrupt the beam with the beam profiler until it had traveled at least half a meter from the chamber, which allowed the spots to further diverge and made it so that all three would not be visible on the photosensitive area of the beam profiler.

To remedy this issue, a window was added to the path of the laser to redirect a portion of the returning laser. The window was inserted into the path of the laser almost immediately after it was reflected off of the mirror directly below the chamber. The beam profiler was set up in the path of the light being reflected by this window to be able to better examine the behavior of the reflections. An image of these three beams taken with the beam profiler can be seen in figure 4.4.

The first avenue of investigation to try to understand the behavior of the three reflections was to see how adjusting the tilt of the reference mirror would impact the relative position of these three beams. It had been noticed when using the laser viewing cards that the beams would converge and diverge as the reference mirror was tilted. As the reference mirror was tilted, the leftmost spot observed in figure 4.4 would not move. At the same time, the center and rightmost spots would move and also converge/diverge from each other.

By adjusting the tilt of the window, and blocking different elements of the beam, we found that the left and rightmost spots were originating from different optical elements. It was found by blocking the laser from reaching the PBS inside the chamber then all three spots would disappear, but by blocking the path between the PBS and the reference mirror the center and rightmost spots would disappear, but not the leftmost.

While the sources of these two unexpected beams were never conclusively proved, the working idea was that the rightmost spot was coming from the laser reflecting off of the back side of the reference mirror. This was due to the fact that it was found that some of

the laser power was being transmitted through the new reference mirror. We thought that this rightmost spot may have been caused by this transmitted laser power being internally reflected by the back surface of the mirror and returning to the chamber. The source of the leftmost spot was thought to be from the PBS since interrupting the path between the PBS and the reference mirror, or the PBS and the oscillator mirror would not interrupt the beam, but interrupting the path between the mirror directly below the chamber and the PBS would interrupt this beam. Ultimately, due to the sufficiently large divergence between these three beams, it was decided that it would not be worth trying to remove the two unwanted beams when they could be physically interrupted without disturbing the beam coming from the front face of the reference mirror.

This led to one of the changes made to the optical bench. While the divergence between these three beams was relatively large and the two unwanted beams should not have been able to reach the PDs, it was decided to add an iris (between PBS#1 and the steering mirrors on the lasers return path) that could be used to physically interrupt them and remove them entirely from the rest of the optical system.

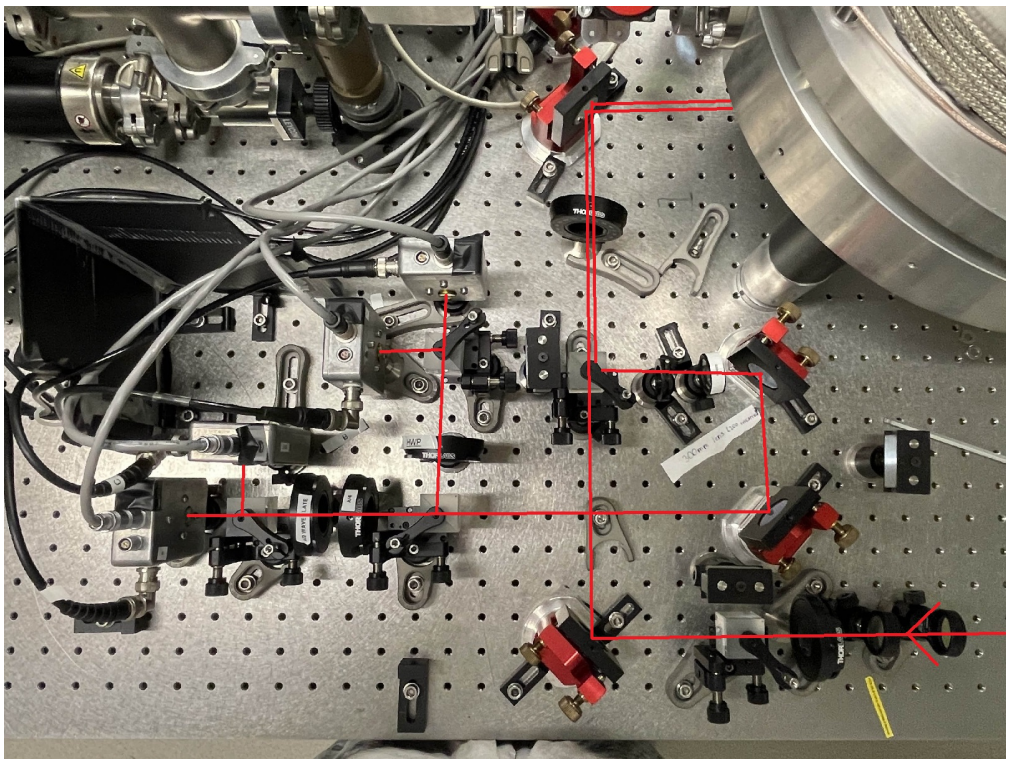

Figure 4.5: Image of the optical bench after a series of changes and upgrades to restore the experiment to working order and to make aligning the system significantly easier. The laser path is drawn on in red with an arrow indicating where the laser is entering the image from.

At the same time, it was decided to make a larger upgrade to the optical bench. Previously, the mirror used to steer the beams returning from the chamber was also the mirror used to send the beams to the chamber. The fact that the mirror would affect both the incoming and returning paths of the laser, and the fact that there was only one steering mirror, made it more difficult than was ideal to steer the beam when the system needed to be realigned. The steering mirror was also located in a part of the experiment that was somewhat difficult to physically reach and adjust, particularly without accidentally blocking the beam. It was decided to move the PBS on the bench and add two new steering mirrors that would be easily accessible accessible. This would make it far simpler to adjust the position of the returning

beams, in particular without affecting the path of the beam going to the interferometer since now only the returning beams would be interacting with the steering mirrors.

The iris that was added to the optical bench can be seen in figure 4.5. However, introducing the two steering mirrors created a new problem, as the path length of the beam had been increased from the previous setup of the optical bench, allowing the beam to diverge more than it had previously, making it larger than the photosensitive area on the PDs. To counteract this, a focusing lens was added immediately after the iris.

Figure 4.6 shows the updated layout of the optical bench after these changes had been made.

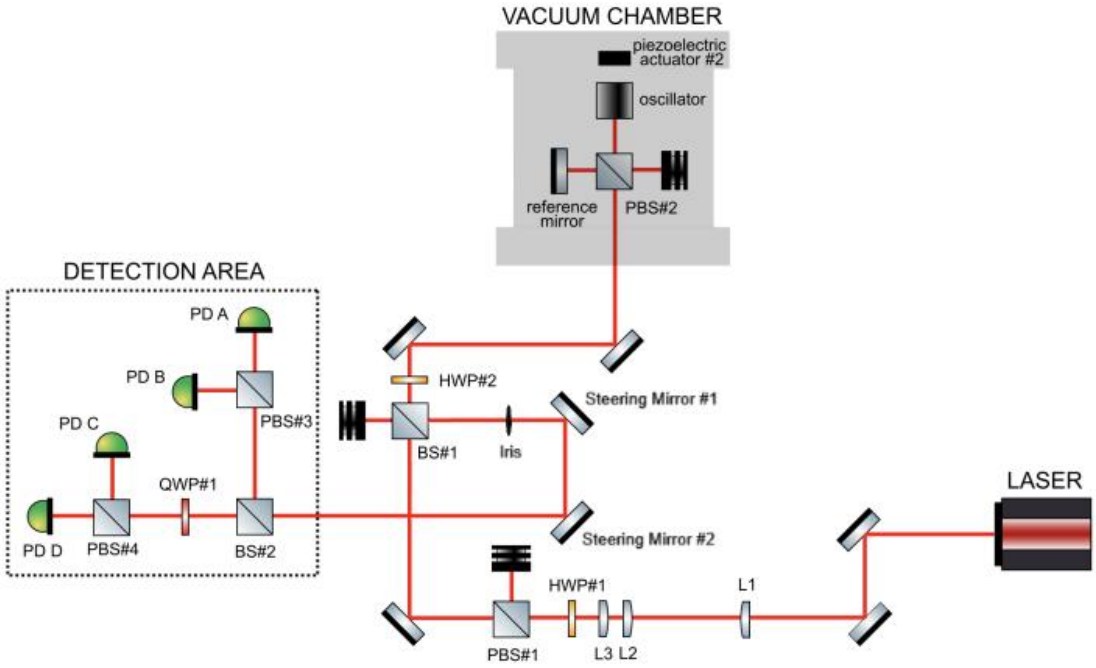

Figure 4.6: Updated version of the optical layout from figure 2.6 after the changes made during the thesis work.

Once these issues had been solved, the optics had to be properly realigned before data collection could begin again. While the steering mirrors could be used to make small corrections, the best way to establish a well-aligned starting point would be to manually move the PDs. The motive behind this was that the steering mirrors and the tilt adjustments on the BSs in the PD area should be near the middle of their adjustable ranges so that each optical element could be adjusted in either direction in the future alignments. Once this alignment process was completed, the experiment was now able to be more easily aligned than previously and would be able to be safely heated and returned to normal temperature without adhesive failure.

After this point, data collection was done for multiple months without having to make any changes to the experiment or having to solve any major problems. Most of the experimentally useful data collected for this thesis work was done during this period.

4.3 Laser Power Problems

Ensuring the PDs were getting enough power to nearly saturate the photodiodes from the laser was a concern throughout the duration of the experiment, as by using the full data

acquisition range acquisition noise could be reduced. A stronger signal leads to a higher signal to noise ratio which results in lower acquisition noise.

In September 2024 it had been noticed that the power across the PDs was substantially lower than expected. We first made sure the power loss was not an alignment issue, and found that this was not the case. By measuring the total power collected across the PDs, as can be seen in figure 4.7, we were able to establish that the laser power was degrading with time. The largest drops in measured voltage correspond to period of time where data were not being collected, and so laser degradation appears as a jump due to lack of data collection over some time, and are marked in the figure.

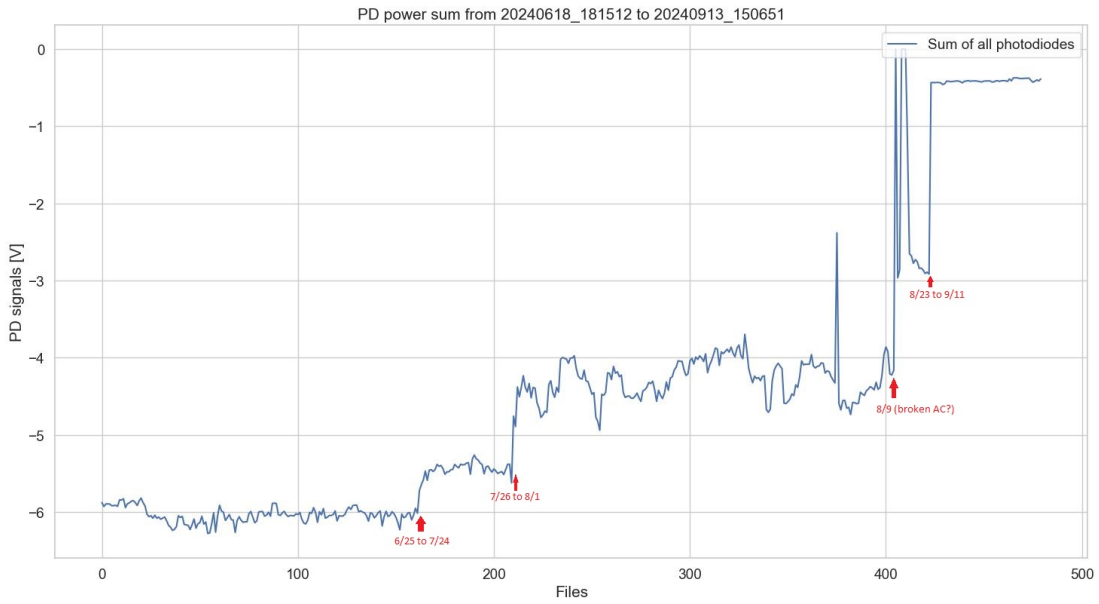

Figure 4.7: Decay of the sum of the voltage measured by the PDs over time. Data was decimated to include a single data point per 20 minutes of data collection. The PD output here is inverted so that more negative values represent higher laser power. Periods of longer pauses in data collection are marked by red arrows.

Once it was clear that the laser power was decaying on its own tests were done to see if the power could be increased to levels suitable for thermal noise measurements. The first step was to adjust HWP#1 to maximize the power reaching the experiment from the laser. This increased the power that was being transmitted through the PBS from around 4.0mW to 26.2mW, which was still insufficient. Since increased power decreases shot noise, in order to continue collecting data with low enough noise to see the resonance peak, the power was going to have to be increased again to continue with data collection.

We tried to recover the lost laser power by adjusting the crystal temperature and the current settings of the laser. During the data collection up to this point these values had been set at 26.99C, which would fluctuate some with ambient temperature effects, and 1.055A.

The crystal temperature had been varied first, as can be seen in 4.8a, which caused large fluctuations in power as the temperature was being adjusted, but did not seem to yield any significant change in power output after it stabilized. Leonardi et al. 2018 [25] was referenced to understand which regions of power and current would give the best results in obtaining higher power output. The temperature had been increased from the initial 26.99C to 30.10C, with an additional increase to 30.20C after it had decayed to 29.90C without any notable effect.

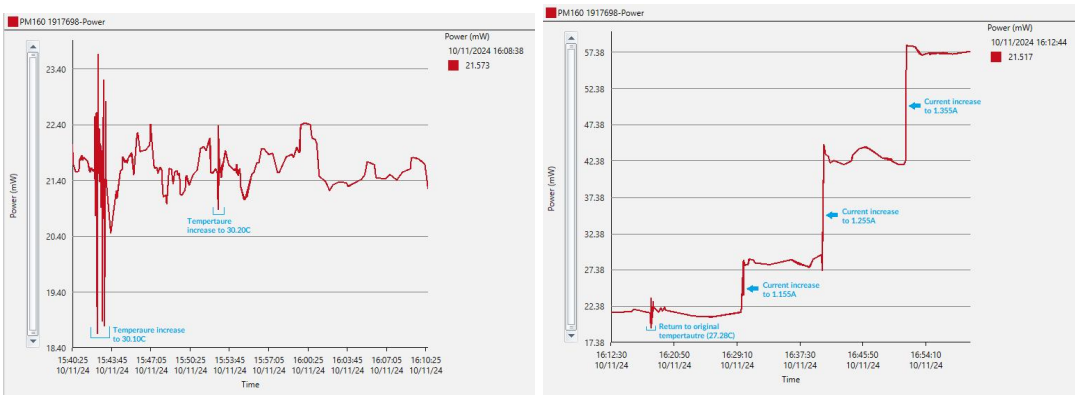

(a) (b)

Figure 4.8: Left (a): Measured power output of the laser when crystal temperature was adjusted. Right (b): Measured power output of laser when current was adjusted.

Next, the current was adjusted to see if this would have an impact on the laser power. As can be seen in 4.8b, this did have a large impact on the power output of the laser. This increase in power still resulted in a lower laser power than had been measured at the beginning of this thesis work, but showed that the power could be increased to a level that was deemed acceptable for more data collection for a period of time, but further decay of the laser power meant that data collection had to be stopped eventually.

5 Results and Discussion

After having made the changes discussed in the previous chapter we were able to collect experimental data, which now needs to be analyzed and discussed. The previous work done on this experimental setup established the ability of the experiment to estimate effective temperature T_{eff} at room temperature. However significant improvement could be made to the consistency of T_{eff} and investigation needed to be done into how the change of thermodynamic temperature would impact T_{eff}. The analysis done for this thesis work aims to establish if the changes made to the experimental setup impacted, ideally improved, the experiment's ability to do so, and to see how this ability to estimate T_{eff} changes at different equilibrium temperatures.

5.1 Behavior at Room Temperature

Measurement of the response of the oscillator to thermal noise requires high displacement sensitivity since for the first longitudinal resonant mode, where thermal noise theoretically is the main driver of the behavior we would observe, an oscillator with a 0.1kg mass, at 300K, and for a frequency of 1400Hz would experience a displacement of 1.45×10^{-13}m. The lowest the continuum of the PSD has been observed to be near the corresponding resonant peak is around $10^{-29}\frac{m^2}{Hz}$, which is two orders of magnitude lower than the typical peak max of around $10^{-27}\frac{m^2}{Hz}$ that is induced by this displacement. While this makes the resonant peak easily observable, it also means that any unexpected noise contribution to the region of the PSD we are most interested in (around 1400 Hz) can raise the continuum of the noise in that region above the resonant peak, making estimation of T_{eff} impossible.

One of the main tests of the ability of the experiment to properly investigate the behavior of thermal noise is for the oscillator to have consistent behavior at equilibrium temperature. So here we are interested investigating how stable this behavior is over time using T_{eff}, as it represents the energy stored in the first longitudinal resonant mode of the oscillator.

The previous thesis work on this project collected data at the ambient temperature of the lab, noted as $\sim 296K$, as seen in figure 5.1 [22]. During this period of data collection, a maximum change of $\sim 60K$ can be seen between the points. However, it is possible that after some of the changes made to the experiment during that work improved the stability of the effective temperature (so corresponding to the blue region in figure 5.1), and that this could have been shown if data had been collected for a period of time. The purpose of much of this previous work was to make changes to the experimental setup to try to reduce noise, in particular noise from the mechanics used to hold the reference mirror of the interferometer. The effective temperature did appear to fluctuate less in later trials based on the limited data in the blue section of figure 5.1, but a maximum change in the effective temperature $\sim 55K$ can still be observed across the larger, later section (in orange) where work had already been done to try to reduce noise from mechanical components.

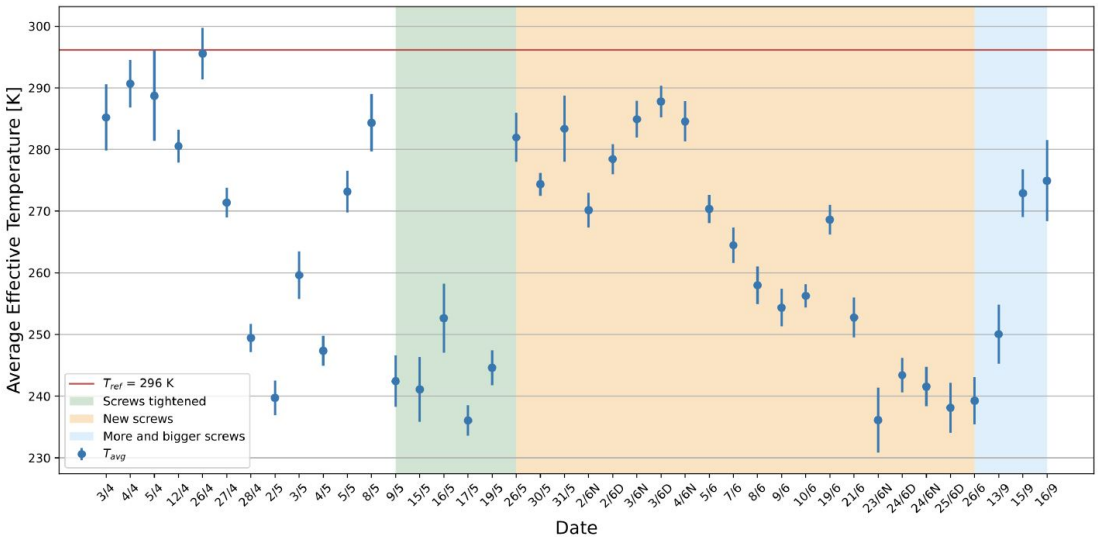

Figure 5.1: Effective temperature calculated and plotted during the previous thesis work on this experiment, each point represents the average T_{eff} over each calendar date, with the error bars representing the standard deviation of the mean $\sigma/\sqrt{N}$, where N is the number of T_{eff} values averaged. The red line represents the average thermodynamic temperature of the experiment over the same period of $\sim 296K$. The different periods corresponding to the different color background reflect changes made to the type of/torque used to tighten the screws securing the flange that holds the oscillator to the mechanical filters. The change to the screws is not of interest to this thesis work, this figure is included to show how T_{eff} drifted over time in previous work. Figure from [22].

5.2 Behavior at Different Equilibrium Temperatures

In the previous work, data collection was only done at room temperature $\sim 297K$. We wanted to investigate the behavior of the experiment at different equilibrium temperatures in this work to see how the measured T_{eff} would change. We wanted to understand the relationship between thermodynamic and effective temperature the experiment would measure, and whether the two would have a simple linear dependence, a linear dependence with an offset, or something else entirely.

In this thesis work we aimed to investigate this same behavior at different equilibrium temperatures, and so a similar figure to figure 5.1 was produced to show the changes in T_{eff} over time, shown in figure 5.2 (and later figure 5.3). All T_{eff} data for each calendar date were averaged to produce each point in the figure to understand the change over time. Data were collected over periods of many days while the experiment was in equilibrium state at room temperature $\sim 297K$ over two different periods of time, as can be seen in the blue regions in figures 5.2 and 5.3. Data were also collected while the experiment was run at different elevated equilibrium temperatures, referred to by the power at which the heater (discussed in section 2.1) was run at; with the yellow sections corresponding to heating of 46W ($\sim 315K$), red to 71W ($\sim 323K$), and orange 26W ($\sim 310K$). Data was also collected for many days for each of these periods, although the 26W period was cut short due to technical issues.

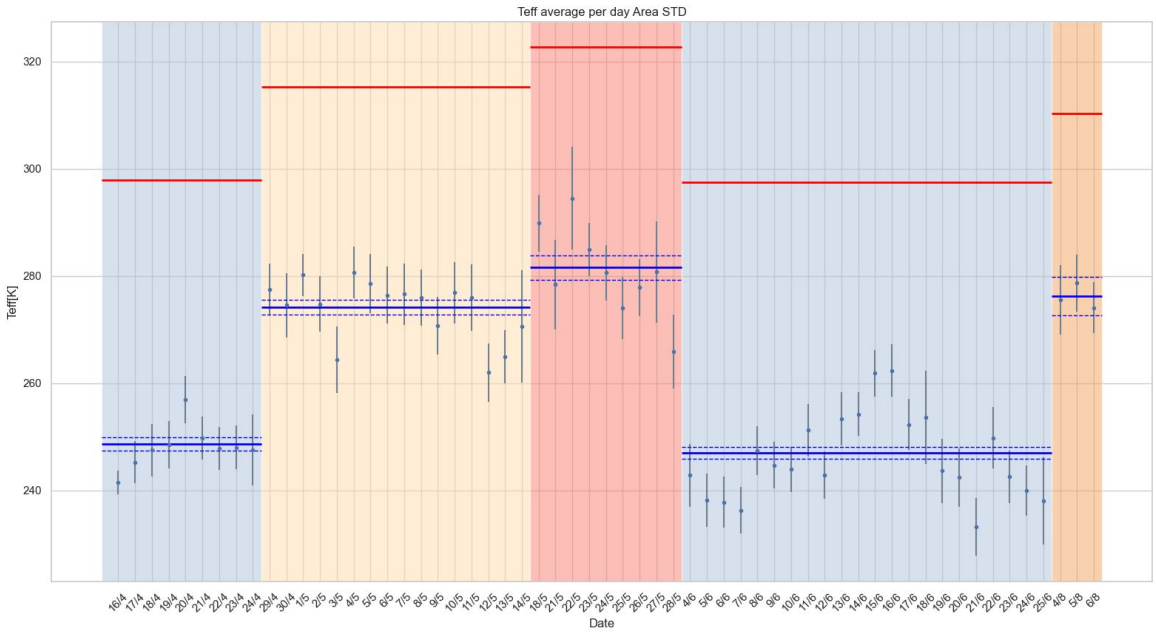

Figure 5.2: Each point in this figure represents T_{eff} averaged over each calendar date. Data was collected while the experiment was at an equilibrium temperature. Each colored region represents results taken from a different equilibrium temperature of the oscillator. The blue regions represent when the chamber was not heated and so the equilibrium temperature was that of the room. For the other regions the chamber was heated; power sent to the heating coil (discussed in section 2.1) was 46W in the case of the yellow region, 71W for the red region, and 26W for the orange region. The red horizontal lines represent the averaged thermodynamic temperature as measured by the thermometers over the same period for the temperature of the oscillator mass. The time series of the thermodynamic temperature was not included as it was too stable to show fluctuations on this scale. The solid blue horizontal lines represent the average all of the effective temperature data that was used to calculate the day averages, with the dashed lines representing the standard deviation of the mean. The error bars on the day points are also standard deviation of the mean.

Data collection at room temperature for this work covered a longer period than that of the previous work while also having a smaller maximum change in T_{eff} over the entire period, only $\sim 30K$ as compared to $\sim 60K$ previously, which represents a significant improvement in the stability of measurements of T_{eff}.

Figure 5.3 was also created where the data used was collected only at night, to investigate if the measured T_{eff} would be more stable during periods where there was no other activity in the lab where the experiment was being conducted. It was thought that it would be worth reducing the amount of data used for each date in order to be able to only use data from when the lab conditions were the most stable. The data used to create figure 5.3 represents two hours of data collection each day; one one-hour period of data collection before and after midnight each night.

It had been observed at multiple different points during the course of the experiment that there was generally less environmental noise during the night time when activity in the lab was at a minimum, so it seemed possible that only using data from the night would result in measurements of T_{eff} varying less over time when only using this data will reduced environmental noise. From what can be seen in the previous figures, cutting the data to a much smaller sample size resulted in a larger scatter in the points, and larger error bars due

to having less data. Whatever advantages using nighttime data here may have led to was offset by having less data to average. This suggests that nighttime measurements do not offer any significant reduction in environmental noise.

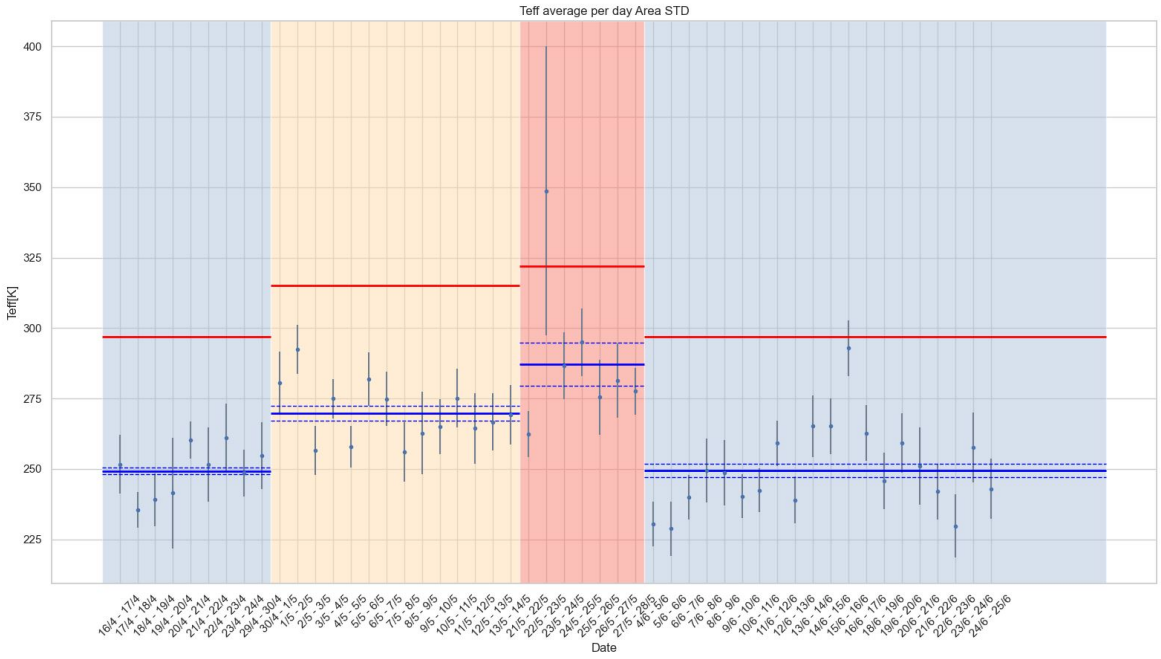

Figure 5.3: Effective temperature measured using data collected during the night time only. Data used was within around 2 hours of midnight in each direction where data exists. The data is formatted in the same way as in figure 5.2.

We then investigated the relationship between the average effective and thermodynamic temperatures for each equilibrium period. As discussed in section 1.4, the equipartition theorem tells us how much energy should be stored in each mode, and in equilibrium it is well understood that the effective temperature should be equal to the thermodynamic temperature. In figure 5.4 two different fits for the average of all of the measured data for these two parameters, T_{eff} and T_{meas} (measured thermodynamic temperature, the measurement of which is discussed in section 2.1), are performed to investigate this.

We first performed an unconstrained linear fit (shown in orange in figure 5.4). We would ideally expect the fit between the two parameters to be linear with a slope of 1 and intercept of 0. The y-intercept of this fit was found to be -163 ± 80K, and the slope was found to be 1.39 ± 0.3. This shows us that a linear fit with a slope of 1 and passing through the original is within 2σ of our fit, which indicates that the T_{eff} measurements are compatible within 2σ of the expected outcome.

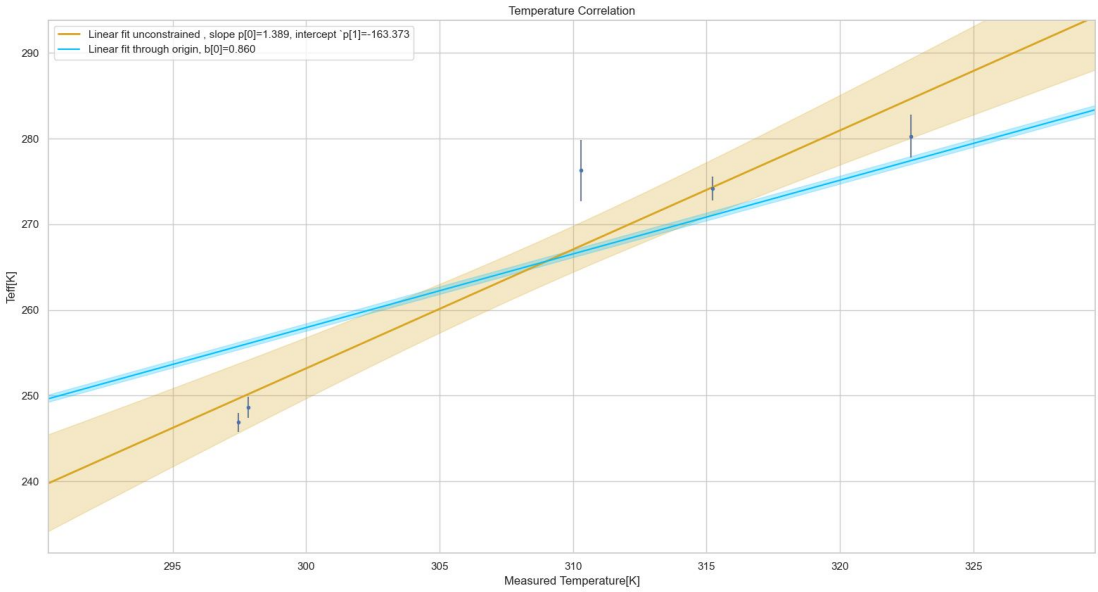

Figure 5.4: This figure contains five points corresponding to the five different data collection runs, showing the average thermodynamic temperature (x-axis) over the period of data collection against the average effective temperature. Each point has error bars representing the standard deviation of the mean on both axes, though the error bars on the x axis are too small to be visible. The orange line represents a simple linear relation with an unconstrained y-intercept of the points, with the orange shaded region being one standard deviation of the fit. The slope of the fit is 1.39 ± 0.3, and the intercept is -163 ± 80K. The light blue line represents a linear fit that is constrained to go through the origin, with the shaded region again representing one standard deviation of the fit. The slope coefficient is 0.860 ± 0.01 for the constrained fit.

The second fitting method we used was a linear fit that was constrained to pass through the origin (shown in light blue) in figure 5.4. Since a linear relationship with an intercept of 0 was expected between T_{eff} and T_{meas} we wanted to investigate how much more poorly the constrained fit would fit the data while still incorporating the expected physical argument of passing through the origin. The slope coefficient was found to be 0.860 ± 0.01 which unlike with the unconstrained fit is not within 2σ of the expected correlation.

A χ^2 test was also performed for each fit, with the value for the unconstrained linear fit found to be ~ 17.9 as opposed to ~ 115 for the constrained linear fit. While neither fit fits the data well, clearly the unconstrained linear fit is the better of the two.

Find a correlation that is compatible with the theory within 2σ is an encouraging sign, but can still be improved. The fact that the unconstrained linear fit fits the data better than the constrained fit indicates the possible presence of an offset in the correlation between T_{eff} and T_{meas}, and could be investigated by acquiring more data at different equilibrium temperatures.

5.3 Parameter Correlation

Although T_{eff} was the main parameter of interest found from the Lorentzian fitting, various other parameters were obtained from this process, as can be seen in section 3.4.

All of the parameters obtained from the fitting of the resonant peak: N_{fit} (the white noise continuum obtained from the Lorentzian fitting process), F_{res} (the frequency of the peak of the resonant peak), and FWHM (the full width at half maximum of the resonant peak),

each had a measurement corresponding with each measured T_{eff}, each corresponding to a 20 second period of fast data that was fit as was discussed in section 3.4. The only exception to this was the phase that indicates the position of the working point ϕ, which was obtained from the fast data at a sampling frequency of 8kHz. The phase was reprocessed to find an average phase for each 20 second period of data.

To understand the correlation between different parameters, Spearman's rank correlation coefficient for each pair was calculated and arranged into a Spearman matrix, allowing for better visualization of different correlations [26]. As the Spearman correlation is a monotonic rank correlation, meaning the correlation strength is based on the monotonic ranking of the two parameters instead of their actual value. This type of fitting can quantify nonlinear correlations, which is useful here where we may find nonlinear correlations. Figure 5.5 shows two selected Spearman matrices found for two different sections of data (sections being the five sections of data shown in figures 5.2 and 5.3), with all relevant matrices shown in appendix figure 5.7.

It is worth mentioning here that a full Spearman matrix for all five parameters cannot be produced for all of the data among the five different heating runs. In order to do so, the phase would have to be unwrapped so that any time the phase crossed the arbitrary 2π--2π threshold the phase would not have a sudden "jump" up or down by 2π. This unwrapping is possible within each of the five data collection runs, but not for all five sections together.

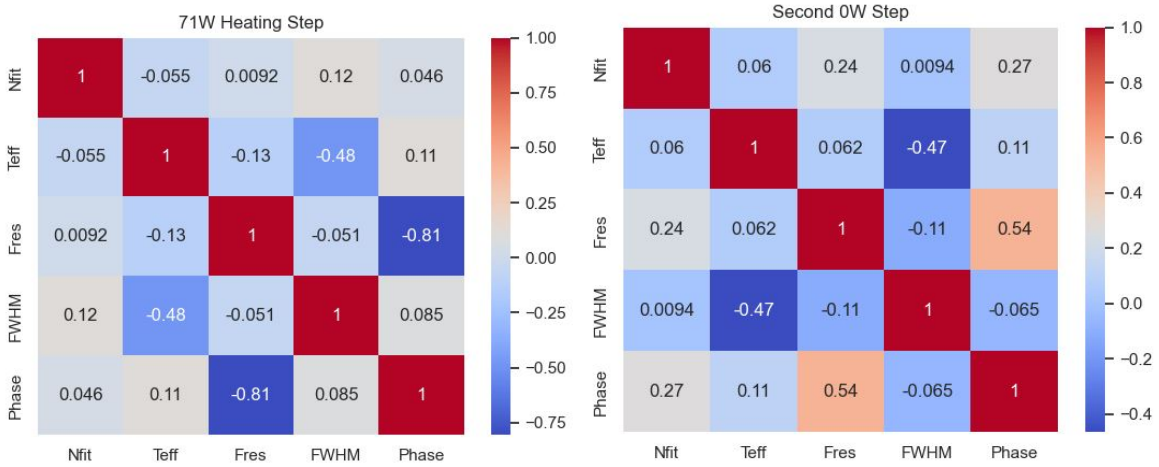

(a) (b)

Figure 5.5: Spearman correlation matrices for the white noise estimate from the peak fitting procedure discussed in section 3.4, N_{fit}, the effective temperature T_{eff}, the frequency of the resonant peak F_{res}, the full width at half maximum of the peak (FWHM), and the phase of the working point ("Phase" in the figure but elsewhere referred to as ϕ). Correlation matricies for all five data collection periods can be seen in the appendix in figure 5.7. (a) Uses data from the section of data collection where the chamber was at equilibrium temperature while heated with the heater at 71W, which corresponds to the red section of figure 5.2. (b) Uses data from the second section of data collection where the chamber was at equilibrium temperature while at room temperature (with the heater set at 0W), which corresponds to the second blue section of figure 5.2. For both figures the red squares are high positive correlation, blue is high (relative) negative correlation.

The most significant correlations shown here are the correlations between FWHM and T_{eff} and between phase and F_{res}, with all other pairs of parameters having a correlation of less then 0.40 for all periods.

The anticorrelation between FWHM and T_{eff} was consistently around -0.50 for all data sets except the final 26W heating run, where the correlation still existed but was about half the magnitude of the other sets of data (as can be seen in the appendix in figure 5.7). This is likely primarily caused by the fact that during the final (26W) heating step (shown in orange in figure 5.2) the chamber was not in as stable an equilibrium state due to issues with lab climate control. This correlation was not expected as the FWHM does not need to change in order for T_{eff} to change. This is a persistent feature of this experiment though and (again with the exception of the 26W heating run) this correlation is stronger than what was reported in the previous work, with a value of -0.38 [22]. This will need to be explained in future work if it persists.

The correlation between phase and F_{res} gave generally consistent results, with one major exception. For four of the five data collection periods (as exemplified in figure 5.5b), the Spearman analysis gave a large positive correlation, ranging from 0.54 at the lowest to 0.98 at the highest (as can be seen in appendix 5.7). A strong correlation was expected, as an increase in temperature would result in a progression of the working point, while also reducing the resonant frequency due to softening of the oscillator with increased temperature. For the remaining section of data, corresponding to the 71W heating run (as can be seen in figure 5.5a), the correlation was of similar magnitude, but negative instead of positive, with a value of -0.81.

It is not clear why this change in correlation sign occurred. As can be seen in figure 5.6 the phase and resonant frequency follow the same trend for approximately the first third of the dataset. This positive correlation stops and appears to reverse for the rest of the data collection period. This behavior was not seen in any other dataset, where all other comparisons between phase and F_{res} showed a positive correlation between these two parameters.

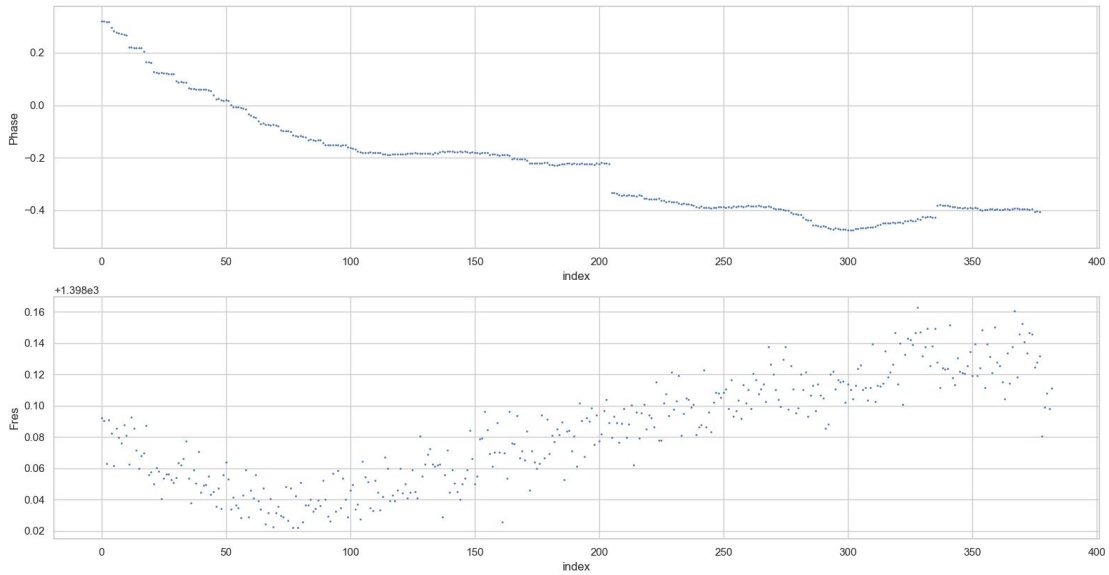

Figure 5.6: This figure shows the phase (top) and fitted resonant frequency of the first longitudinal mode (bottom) for the 71W heating step vs index (index is chronological order the points were taken, considered to be more useful for visulizing the data than resonant frequency vs date). Points here are selected to be only the one passing the χ^2 threshold.

In the previous work on this project the Spearman coefficient for the correlation between phase and F_{res} was reported to be -0.89 [22]. This correlation was also the strongest correlation of any of the parameters pairs that also appear in this work; however, it was of opposite sign

of four of the five values reported here, as can be seen in figure 5.7. The recording of the phase is based on the electronic recording of the full phase of the laser by the four photodiodes, and the sign of it is a convention based on how the signals for the four PDs are processed. It is possible that during the upgrade work done to the optical bench, a change was made that resulted in the phase being of opposite sign, such as the rotation of a half waveplate or quarter waveplate or the accidental swapping of PDs during upgrade work, although this would not explain the behavior seen in figure 5.6. It could be possible to check if the correlations between phase and other parameters were also reversed in sign; however, most other correlations with phase reported for this work are close to null, making comparison difficult. The one exception is the correlation between N_{fit} and phase, which is reported to be positive in all cases in this work, and as high as 0.34 for the first 0W data collection period. In the previous work, the correlation reported between N_{fit} and the phase had a value of -0.40, which like with phase and F_{res}, is of opposite sign as in this work, which is further evidence that the work on the optical bench did result in a "flip" in the way the phase changed, so resulting in Spearman correlation coefficients for phase and the other parameters of opposite sign.

The fact that N_{fit} and the phase had a correlation of -0.40 in the previous work was noted as unexpected, and it was speculated that it was caused by some photodiodes being more acutely affected by optical-electronic noise than others. This would result in a correlation between white noise and phase, as more noise would be present when certain PDs were more strongly illuminated due to a change in the phase. As the PDs were removed and put back in place during the upgrades made to the experiment during this work, it is possible an unintended swap of the PDs in a pair led to a reversal of the behavior of the phase.

Another correlation that had been noted as unexpected in the previous work was a correlation between T_{eff} and N_{fit}), which had a correlation value of 0.46. This had been discussed in the work done by Saoncella, where it was stated that this would have had to be due to some other parameter that affected both T_{eff} and N_{fit} that did not have a physical origin, as white noise is not related to the real motion of the oscillator. Work had not been done to try to specifically understand this behavior, but after the work that was done to try and improve the sensitivity of the system (discussion in chapter 4), this correlation no longer appears in any of the data collection runs at any temperature, which is the behavior that had originally been expected, and so this issue appears to be resolved.

The Spearman correlation analysis also resulted in the discovery of "jumps" in the phase of the working point, as can be seen in figure 5.6 around indices 205 and 335. This behavior had also been noted in the previous work by Saoncella [22]. These jumps have not been found to strongly coincide with any other physical behavior of the system, although in some cases it was found that the correlation between phase and other parameters may change in slope and/or offset after a jump occurred, possibly indicating non-monotonic behavior. Further work on this experimental setup could try to understand what is causing these jumps in phase, possibly leading to further improvements in the sensitivity of the system.

Conclusions

The scientific motivation for this work is to eventually be able to characterize thermal noise out of thermodynamic equilibrium in solids. To this end, we must first demonstrate that we can consistently measure the behavior of a solid in thermodynamic equilibrium. This work was carried out using a quadrature phase differential interferometer using a monolithic aluminum cube and square rod as both one of the mirrors of the interferometer and as an oscillator with the behavior of its oscillations dominated by thermal fluctuations that are well modeled by the equipartition theorem in thermodynamic equilibrium. In the previous work on this experiment, the behavior of the oscillator was characterized by investigating its first longitudinal resonant mode, which was quantified by finding its effective temperature T_{eff}. In the previous work, the behavior of the oscillator was monitored for weeks at an equilibrium temperature of $\sim 297K$ to investigate the behavior of T_{eff}. It was found that T_{eff} was both insufficiently stable, and consistently lower than expected from theory. The peak-to-peak variation in T_{eff} over the course of this work was $\sim 60K$, which needed to be improved to be able to investigate the behavior of the oscillator out of thermodynamic equilibrium.

The first thing investigated as part of this work was the behavior of the oscillator at different equilibrium temperatures by heating the oscillator. The measurements from the photodiodes of the interferometer became erratic after the first data collection at elevated temperature. After investigating it was found that the glue attaching the reference mirror of the interferometer to an actuator had degraded due to heating, leading to the eventual detaching of the reference mirror. This mirror was replaced and the actuator was removed entirely. This was accompanied by other improvements to the experimental setup, including the addition of steering mirrors that could be used to more easily align the system, and the addition of an iris to interrupt extraneous laser reflections. Data was then collected over five periods at four equilibrium temperatures: $\sim 297K$, $\sim 315K$, $\sim 323K$, and $\sim 310K$, with two periods at $\sim 297K$ and one period at each other temperature.

The interferometric output measured during these periods was used to calculate T_{eff}, which allowed us to investigate the behavior of the oscillator. It was found that the variation of the measured effective temperature at each constant thermodynamic temperature was smaller than that found in the previous work, with a maximum variation of $\sim 30K$ within any one period of data collection instead of $\sim 60K$ in the previous work even though this work collected data over a longer period of time. This demonstrated that the changes made to the experiment during this work increased the stability of T_{eff} measurements.

The average T_{eff} of each of the five data collection periods was also compared with the average thermodynamic temperature of each period. Based on theory, T_{eff} is expected to be equal to the thermodynamic temperature, with correlation between both parameters being a line with a slope of 1 and intercept of 0. Two fitting methods were then performed using these two parameters to try and confirm this behavior; an unconstrained linear fit, and a linear fit constrained to pass through the origin. Both fits were found to be poor fits for the data using a χ^2 test, but the constrained linear fit was found to be significantly worse than the unconstrained one. The intercept and slope of the unconstrained fit were found to fit the theory within 2σ, showing that our results were compatible with the theoretical predictions; while this result does not completely exclude compatibility with the theoretical model, it suggests that a more refined model may be needed to correctly interpret the data collected.

Future work can take more measurements at different equilibrium temperatures to see if this compatibility with the theory can be more strongly demonstrated and attempt to further increase the stability of T_{eff} measurements. The increased stability and apparent confirmation of theory for thermodynamic equilibrium also indicates it may be already be valuable to start investigating the behavior of thermal noise out of thermodynamic equilibrium.

References

[1] Matthew Pitkin et al. "Gravitational Wave Detection by Interferometry (Ground and Space)". In: *Living Reviews in Relativity* 14.1 (July 2011). ISSN: 1433-8351. DOI: 10.12942/lrr-2011-5. URL: http://dx.doi.org/10.12942/lrr-2011-5.

[2] Albert Einstein. "Approximative Integration of the Field Equations of Gravitation". In: *Sitzungsber. Preuss. Akad. Wiss. Berlin (Math. Phys.)* 1916 (1916), pp. 688–696.

[3] Michele Maggiore. *Gravitational Waves. Vol. 1: Theory and Experiments*. Oxford University Press, 2007. ISBN: 978-0-19-171766-6, 978-0-19-852074-0. DOI: 10.1093/acprof:oso/9780198570745.001.0001.

[4] Alexandre Le Tiec and Jérôme Novak. "Theory of Gravitational Waves". In: *An Overview of Gravitational Waves*. WORLD SCIENTIFIC, Feb. 2017, pp. 1–41. ISBN: 9789813141766. DOI: 10.1142/9789813141766_0001. URL: http://dx.doi.org/10.1142/9789813141766_0001.

[5] B. P. Abbott et al. "Observation of Gravitational Waves from a Binary Black Hole Merger". In: *Physical Review Letters* 116.6 (Feb. 2016). ISSN: 1079-7114. DOI: 10.1103/physrevlett.116.061102. URL: http://dx.doi.org/10.1103/PhysRevLett.116.061102.

[6] Odylio Denys Aguiar. "Past, present and future of the Resonant-Mass gravitational wave detectors". In: *Research in Astronomy and Astrophysics* 11.1 (Dec. 2010), pp. 1–42. ISSN: 1674-4527. DOI: 10.1088/1674-4527/11/1/001. URL: http://dx.doi.org/10.1088/1674-4527/11/1/001.

[7] R A Hulse and J H Taylor. "Discovery of a pulsar in a binary system". In: *Astrophys. J., Lett., v. 195, no. 2, pp. L51-L53* (Jan. 1975). DOI: 10.1086/181708. URL: https://www.osti.gov/biblio/4215694.

[8] O Jennrich. "LISA technology and instrumentation". In: *Classical and Quantum Gravity* 26.15 (July 2009), p. 153001. ISSN: 1361-6382. DOI: 10.1088/0264-9381/26/15/153001. URL: http://dx.doi.org/10.1088/0264-9381/26/15/153001.

[9] Tianjun Li et al. "Measurements of mechanical thermal noise and energy dissipation in optical dielectric coatings". In: *Physical Review D* 89.9 (May 2014). ISSN: 1550-2368. DOI: 10.1103/physrevd.89.092004. URL: http://dx.doi.org/10.1103/PhysRevD.89.092004.

[10] Scott A. Hughes and Kip S. Thorne. "Seismic gravity-gradient noise in interferometric gravitational-wave detectors". In: *Phys. Rev. D* 58 (12 Nov. 1998), p. 122002. DOI: 10.1103/PhysRevD.58.122002. URL: https://link.aps.org/doi/10.1103/PhysRevD.58.122002.

[11] Wenxuan Jia et al. "Squeezing the quantum noise of a gravitational-wave detector below the standard quantum limit". In: *Science* 385.6715 (Sept. 2024), pp. 1318–1321. ISSN: 1095-9203. DOI: 10.1126/science.ado8069. URL: http://dx.doi.org/10.1126/science.ado8069.

[12] F. Acernese et al. "Increasing the Astrophysical Reach of the Advanced Virgo Detector via the Application of Squeezed Vacuum States of Light". In: *Phys. Rev. Lett.* 123.23 (2019), p. 231108. DOI: 10.1103/PhysRevLett.123.231108.

[13] Horace P. Yuen. "Contractive States and the Standard Quantum Limit for Monitoring Free-Mass Positions". In: *Phys. Rev. Lett.* 51 (9 Aug. 1983), pp. 719–722. DOI: 10.1103/PhysRevLett.51.719. URL: https://link.aps.org/doi/10.1103/PhysRevLett.51.719.

[14] Richard F. Greene and Herbert B. Callen. "On a Theorem of Irreversible Thermodynamics. II". In: *Physical Review* 88.6 (Dec. 1952), pp. 1387–1391. DOI: 10.1103/PhysRev.88.1387.

[15] Peter R. Saulson. "Thermal noise in mechanical experiments". In: *Phys. Rev. D* 42 (8 Oct. 1990), pp. 2437–2445. DOI: 10.1103/PhysRevD.42.2437. URL: https://link.aps.org/doi/10.1103/PhysRevD.42.2437.

[16] A D Brailsford. "Anelastic Relaxation in Crystalline Solids". In: *Physics Bulletin* 24.5 (May 1973), p. 305. DOI: 10.1088/0031-9112/24/5/036. URL: https://dx.doi.org/10.1088/0031-9112/24/5/036.

[17] Mickael Geitner et al. "Low thermal fluctuations in a system heated out of equilibrium". In: *Physical Review E* 95 (Dec. 2016). DOI: 10.1103/PhysRevE.95.032138.

[18] L. Conti, M. Bonaldi, and L. Rondoni. "RareNoise: Non-equilibrium effects in detectors of gravitational waves". In: *Class. Quant. Grav.* 27 (2010). Ed. by Zsuzsa Marka and Szabolcs Marka, p. 084032. DOI: 10.1088/0264-9381/27/8/084032.

[19] Livia Conti et al. "Effects of breaking vibrational energy equipartition on measurements of temperature in macroscopic oscillators subject to heat flux". In: *J. Stat. Mech.* 1312.12 (2013), P12003. DOI: 10.1088/1742-5468/2013/12/P12003. arXiv: 1305.5084 [cond-mat.stat-mech].

[20] Luis Diego. Bonavena. "Commissioning of Quantum Noise Reduction for AdV+ and Study of Non-Equilibrium Thermal Noise". PhD thesis. Università degli studi di Padova, Italy, Padua U., 2024.

[21] Mario Saraceni et al. "A compact, passive setup for low vibration noise measurements in the frequency band (300-2000) Hz". In: *The Review of scientific instruments* 81 (Mar. 2010), p. 035115. DOI: 10.1063/1.3361040.

[22] Giulia Saoncella. "Interferometric measurements and data analysis for the study of thermal noise in solids". Master's thesis. UNIVERSITÀ DEGLI STUDI DI PADOVA, 2023.

[23] Edward Collett. *Field Guide to Polarization*. 1st ed. SPIE, 2005.

[24] Peter L. M. Heydemann. "Determination and correction of quadrature fringe measurement errors in interferometers." In: *Applied optics* 20 19 (1981), pp. 3382–4. URL: https://api.semanticscholar.org/CorpusID:43774931.

[25] Matteo Leonardi et al. "Efficient second harmonic generation with compact design: Double-pass and cavity configurations". In: *Laser Physics* 28 (Nov. 2018), p. 115401. DOI: 10.1088/1555-6611/aad84d.

[26] R Artusi, P Verderio, and E Marubini. "Bravais-Pearson and Spearman correlation coefficients: Meaning, test of hypothesis and confidence interval". In: *The International journal of biological markers* 17 (Apr. 2002), pp. 148–51. DOI: 10.5301/JBM.2008.2127.

Appendix

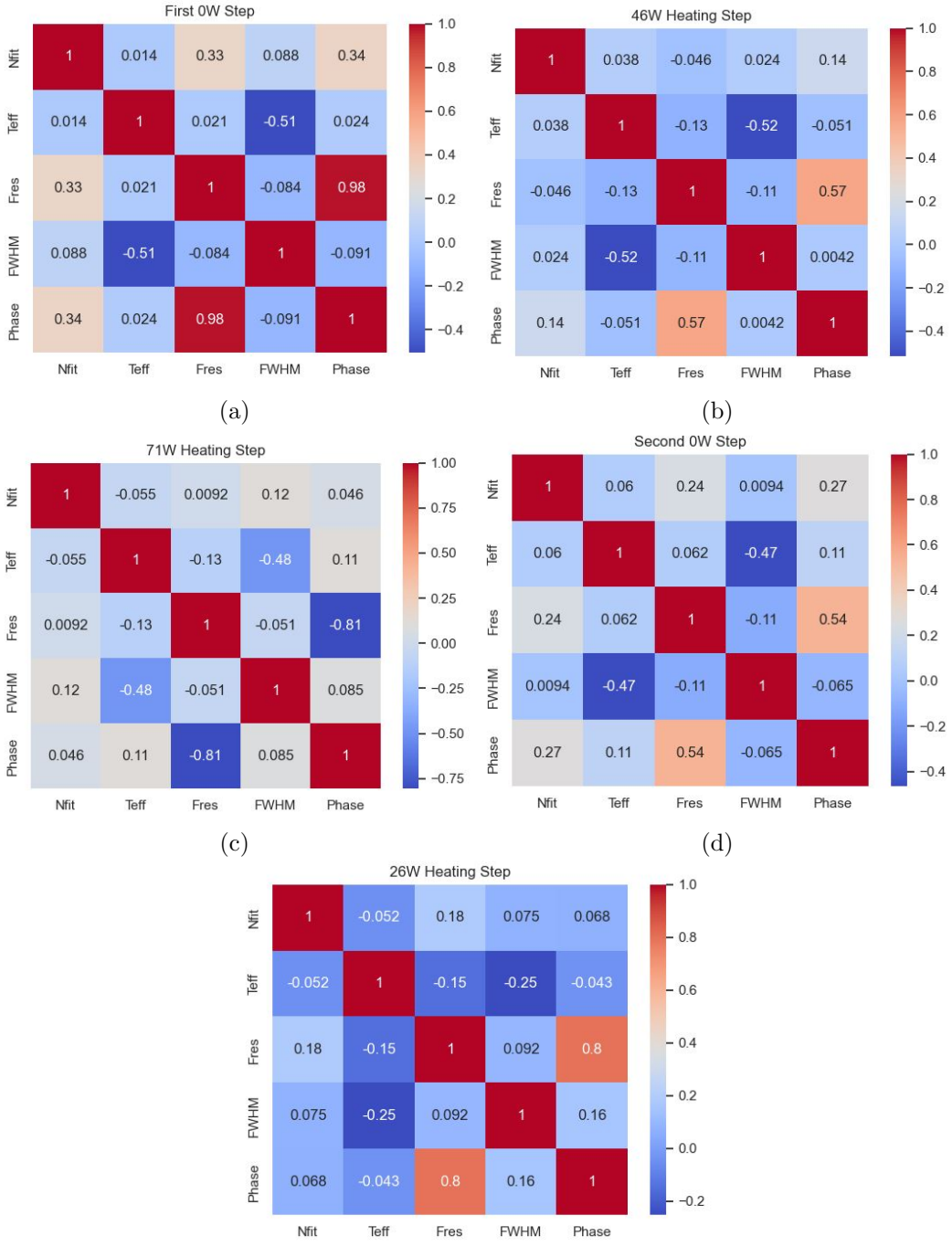

Figure 5.7: Spearman correlation matricies (dicussed in section 5.3) for the all of the same parameters as shown in figure 5.5; N_{fit}, T_{eff}, F_{res}, FWHM, and phase (ϕ). The figures from figure 5.5 can also be seen here, with only two shown in the section in the interest of showing only relevant examples for compactness. Each matric here represents a period of data collection at equilibrium and corresponds with each section of data that can also be seen in figure in figure 5.2 with subfigures (a-e) representing each in chronological order. For all figures red represents the largest postive correlation and blue the largest negative correlation.